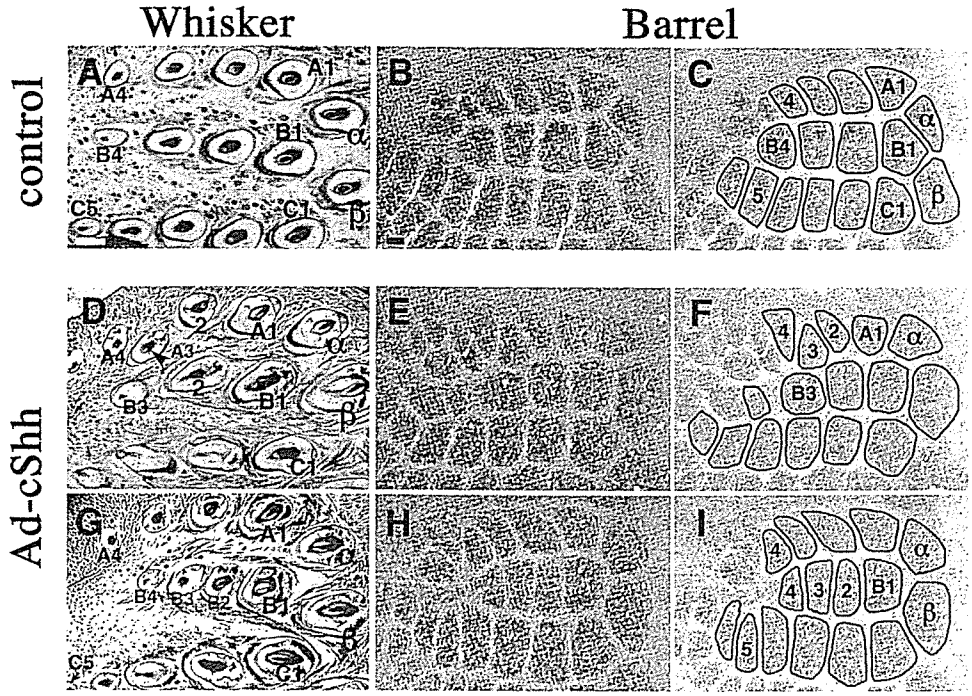

Fig. 6. Alternation of the whisker positions are represented topographically in the barrels. (A) Enlarged view of the dorsal whisker pattern in a control mouse. (B) Barrel pattern corresponding to the whisker pattern shown in (A) visualized by CO staining. (C) Part of the pattern revealed in (B) drawn schematically. (D, G) Disorganized whisker pattern. These mice were infected with Ad-cShh at E10.5 and E11.5 and then analyzed at P25 and P20, respectively. Some of the whiskers are abnormally positioned (red letters and arrowhead). (E, H) Barrels in the cortex contralateral to (D) and (G), respectively. (F, I) Barrels in (E) and (H) drawn schematically. Barrels that are related to abnormally positioned whiskers are displaced (red letters and closed red circles). Thus, the barrel pattern is a topographical replica of the whisker pattern. Bar 0.1 mm.

positive for cShh (data not shown). Most of the pups with an abnormality were killed by the mother or adoptive mother within a day of birth, while those spared survived for months. Four pups with disoriented and supernumerary whisker patterns were viable beyond the critical period for barrel patterning (P6) and were used for barrel-pattern analysis. As a control experiment, we infected embryos with Ad-lacZ. We found sustained expression of β-gal activity even at P2 (data not shown). But none of the pups showed a whisker pattern abnormality (nine pups obtained from three pregnant mothers).

3.4. Supernumerary whiskers are topographically represented by extra barrels

Supernumerary whiskers were induced by infecting embryos with Ad-cShh at E10.5, and analyzing the outcome at P25. One extra whisker positioned between B3 and C3 was termed the C′3 whisker, and other extra whiskers positioned above C5–7 were termed C′5–7, according to the nomenclature [62]. Extra whiskers were also seen between rows D and E (Fig. 4A and D). These supernumerary whiskers were positive for LUXOL Fast Blue, which stains myelinated nerves (light blue) as well as whisker and hair cortex (purple), indicating that the trigeminal nerve targeted supernumerary whiskers. The barrel pattern of the mouse was analyzed by CO staining (Fig. 4B and E). Extra barrels were seen between B3 and C3, above C5–7 and between rows D and E in the contralateral side of the altered whisker pattern. The other side of the whisker pattern had little or no effect on the formation of the ipsilateral side of the barrel pattern. Thus, the barrels were a topographic reflection of the supernumerary whiskers. Insertion of extra barrels led to a decrease in the size of the surrounding barrels, but these additional barrels were indistinguishable from their neighbors. In a separate experiment, alteration of the barrel pattern was also demonstrated at the cytoarchitectural level by Nissl staining of cortical neurons (Fig. 5E). Recently, it has been reported that the patterning of thalamic afferents and the reorganization of cortical neurons are genetically separated [21]. In this study, we have shown that extra barrels induced by supernumerary whiskers caused by cShh exhibit both thalamic afferents and reorganization of the cortical neuron.

3.5. The barrel pattern follows whisker shifts

In some cases, mouse embryos infected at E9.5 to E11.5 showed alternation of whisker positions. One mouse was infected with Ad-cShh at E10.5 and examined at P25. In this mouse, a whisker termed A3 was displaced ventral to its normal position (compare Fig. 6A and D). The A3 barrel of this mouse was triangular in shape and was

shifted anteriorly to its normal position (Fig. 6C and F) when visualized by the CO staining method. In another case, a mouse was infected at E11.5, and was examined at P20. The whisker positions of this mouse, termed B2, B3 and B4 whiskers, were shifted caudally such that the B4 whisker was located at the B3 position of the control mouse, and the normal position of the B4 whisker was left vacant (Fig. 6G). The B4 barrel of this mouse was located between A3 and C3/4 (Fig. 6I), where the B3 barrel is positioned in the control mouse (Fig. 6C). Thus, the topography of the whisker patterns were represented precisely by barrel fields.

4. Discussion

4.1. Expression of the follicular marker genes and induction by ectopic expression of cShh

We studied the expression of follicular marker genes in control mice and the induction of these genes after infection with Ad-cShh in the whisker pad region. The *Shh* of chicken and mouse are functionally substitutable in our results, which confirms a previous study [54].

The expression of *Bmp4* was restricted to the mesenchyme beneath the follicular placode where *Bmp2* was expressed. The expression of *Bmp4* is intriguing because the whisker develops through the interaction of the epidermis and the mesenchyme where *Bmp4* is expressed. *Bmp2* and *Bmp4* are orthologous genes of the *Drosophila decapentaplegic* (*dpp*) family, a target gene of the hedgehog. Although *Bmp2* is known to be a target gene of *Shh* in the developing limb bud [17,31,36], the expression of *Bmp2* in developing hair follicles is independent of *Shh* [58]. Our study also showed that the expression of *Bmp2* was unchanged in the developing whisker after infecting with Ad-cShh. These results indicate that transcriptional regulation is different between the limb bud and the whisker follicle. *Bmp2* and *Bmp4* are closely related [16], and the expression of *Bmp4* is also independent of *Shh* [58] in developing hair follicles. *Bpm4* was, however, induced by Ad-cShh 1 day after infection, and the expression might play an important role in whisker development (see below).

At E13.5, *Ptch*, *Ptch2* and *Gli1* were restricted to the follicular mesenchyme and matrix region. However, at E11.5, expression of the three genes was broadly distributed. The broad expression of *Ptch*, *Ptch2* and *Gli1* may indicate that the transcriptional initiation of the three genes is independent of *Shh*, and *Shh* enhances the expression of *Ptch* and *Gli1* around the follicle after the formation of the whisker placode. This coincides with previous reports that the expression of *Ptch* and *Gli1* is dependent on *Shh* and the expression of *Ptch2* is independent of *Shh* [9,58]. Alternatively, the broad expression of the three genes may be a reflection of the diffusion of *Shh* [17]. All three genes, however, were positively regulated by ectopic expression of cShh.

Shh itself was not induced in the interfollicular region by infection with Ad-cShh. Thus, unlike in the spinal cord, in which *Shh* is autoregulated [37], infection of Ad-cShh was insufficient for induction of *Shh*. Considering the positive feedback loop between *Shh* and *Fgf4* in the chicken limb bud [31], some molecules, such as *Fgf* family members, are necessary to induce and maintain the expression of *Shh*. Among the *Fgf* family members, *Fgf5* is a regulator of the hair growth cycle [23]. *Fgf1*, *2* and *7* are expressed in developing hair follicles [46,48,55]. The induction and maintenance of *Shh* may also require the expression of Wnt signaling [24,29,52].

4.2. Whisker patterning regulated by Shh

Whisker development occurs through the interaction of the epidermis and the mesenchyme and involves many signaling molecules. Modulation of these genes in utero would open a way to investigate the precise molecular mechanism leading to whisker formation. Among these, *Shh* is expressed at the developing hair follicles and is essential for their formation [9,58]. It is also sufficient to induce another cutaneous appendage, chicken feather bud [40]. Therefore, we transfected *Shh* through an in utero operation in an attempt to create an extra placode of whiskers.

In *Shh* knockout mice, the expression of other signaling molecules, *BMP* and *Wnt*, and the formation of the early stage of hair follicles were not impaired [9,58]. Our gain of function analysis, however, showed that *Shh* induced supernumerary whiskers with sever distortions of the original pattern (Figs. 4 and 5) or just a minor shift (Fig. 6D and G). At present, these abnormalities are not predictable in terms of dose of Ad-cShh or the stage of infection. Whiskers in the control usually consist of five rows and four straddlers. The two dorsal rows (A and B) of the facial whiskers are on the lateral nasal prominence, while the three ventral rows (C, D, and E) are on the maxillary prominence [68]. Interestingly, the supernumerary whiskers in the mouse line established by Van der Loos tend to be located between different prominences, one between the medial and lateral nasal prominence, the other between the latter and the maxillary prominence [62]. In this work, supernumerary whiskers appeared not only between the prominences, but also in another part of the whisker pad region after infection with Ad-cShh. We also note that the incidence of whisker induction and the number of whiskers induced were limited compared with the incidence of polydactyly after Ad-cShh treatment (Table 3), while infection was seen throughout the epidermis. The small increment in supernumerary whiskers may arise from transient and/or low level expression of *Shh* in our operation. It remains to be clarified if induction of extra whiskers by ectopic expression of *Shh* was

accompanied by the expression of *Wnt* and/or *Fgf* family genes.

A possible role of *Shh* in pattern formation is suggested in the developing retina. In both vertebrates and invertebrates, development of the retina is driven by the morphogenic furrow, which is regulated by the expression of *Shh* or *hedgehog*, respectively [22,34,43]. Thus, the patterning mechanism of the whisker may share common aspects as found in the retina, although the patterning of early hair follicles is normal in the *Shh* mutant [58]. In the whisker patterning, however, we observed that the interfollicular spacing (Fig. 2B) tended to be spared on infection with Ad-cShh. cShh induced *Bmp4*, which has an inhibitory effect on whisker development [8]. Thus, the perturbed balance of *Shh* and *Bmp* might disrupt the original whisker pattern, possibly through induction of *Fgf* and/or *Wnt* signaling, which is important for whisker development [52,64,69], resulting in the generation of new rows. The precise molecular mechanism of whisker pattering can be investigated by the method described in this paper.

We always found altered whisker patterns accompanied by abnormal limbs. These unintended abnormalities might be circumvented by restricting infection of Ad-cShh to the follicular region, but the embryos could hardly be seen through the non-transparent uterus at the time we operated on the embryos (E9.5 to E11.5). An ultrasound backscatter microscopy system, which visualizes the embryos in the uterus, may solve this problem [32].

4.3. Altered whisker patterns are topographically replicated in the barrel pattern

In this study, we have shown that supernumerary whiskers induced by Ad-cShh are topographically represented by extra barrels. This is the conclusive evidence directly supporting the instructive role of the extrinsic mechanism. Various methods have been used in an attempt to change the peripheral pattern of input. Andres [4] implanted whiskers into the whisker pad region of postnatal mice, which led to the formation of extra barrels. However, their positions were aberrant and did not reflect the whisker pattern. Van der Loos established mouse lines with supernumerary whiskers through selective breeding [62]. Their mice had additional topographically positioned barrels. However, the genetic locus responsible for this phenotype has not yet been identified. Therefore, it is not known if the patterning of the whiskers is solely affected in their lines. Cauterization of whiskers after birth is usually carried out for the study of plasticity. This operation will not change the pattern of the barrelettes, which is already established by the day of birth [6]. We induced supernumerary whiskers by in utero operation using Ad-cShh, so that the whisker pattern was altered prior to the establishment of the barrelette patterning at the brainstem level. Our method may be a new tool for the analysis of barrelette pattern formation.

We found various types of abnormal whisker patterns after infection with Ad-cShh. These were reflected as a topographical map in the barrel cortex. Ad-cShh is not likely to affect the patterning of barrels directly because *Shh* is not expressed in the somatosensory cortex.

Recent advances in the study of barrel patterning suggest that several genes coordinate to produce a functional map. For the segregation of thalamocortical afferents, cAMP plays important roles [1]. The metabotropic glutamate receptor mGluR5 is essential for barrel segregation within a row, and phospholipase C-β1 and cortical NR1 for reorganization of cortical neurons (reviewed in Ref. [18]). Analysis of the adenylyl cyclase I mutant suggests that the segregation of thalamocortical afferents and the topology of barrels are independent [1,66]. This result can be interpreted as follows: first, a cortical map may be organized by an intrinsic mechanism independent of peripheral input; second, a normal peripheral pattern may eventually instruct a cortical map. Thus, it would be interesting to apply the method described in this study to the barreless mutant and to investigate the functional map.

Cortically expressed ephrin A5 does not regulate a gross barrel topology, but can affect segregation of the thalamocortical neurons and the barrel functional map [51,61]. It remains to be clarified if the expression of Eph receptors in the VB complex was altered in our mice.

Our results indicate that a new whisker pattern can also be produced using these mechanisms, leading to barrel segregation and a reorganization of cortical neurons (Fig. 5E and F). Our results, however, do not rule out the intrinsic mechanisms of barrel patterning, which are independent of peripheral input. It would be interesting to use electrophysiological analysis and in vivo imaging to observe the altered barrel patterns produced in our study.

It is of note that visual orientation modules can be induced in the auditory cortex [57] and that close examination of the visual map induced in the auditory cortex revealed inaccurate topography along the isofrequency dimension of the cortex [53], suggesting the existence of an intrinsic mechanism as a rough map [2,12]. This initial map may be further refined depending on neural activity, leading to a replicated map of the peripheral pattern [19,26,56]. Thus, our new method would make it possible to see how peripheral afferents interact with central dendrites to establish a topographic map at a more detailed molecular level.

We note that the interfollicular distances changed in some case (Fig. 6G) and this topology was also replicated in the barrel (Fig. 6I). This result is different from a report based on lesion studies, in which barrels related to cauterized whiskers were narrowed and invaded by nearby intact barrels [47,63]. Induction of the septa is not likely to be derived from the abnormal interfollicular region, because these regions are not represented by the barrel region

[44,49]. At present we have no idea of the mechanism of this phenomenon. A mathematical model, however, predicts that the projection from the medial division of the posterior nucleus POm to the septa region is important in yielding a patchy barrel pattern [60]. The paralemniscal pathway and the leminiscal pathway differently process the information from the whisker [3]. However, the developmental roles of the pathways for barrel patterning still have to be clarified.

Acknowledgements

We thank Drs. N. Tamamaki, K. Yuasa, S. Hattori and T. Inoue for technical advice and critical discussions, and Drs. H. Ogura, B.L. Hogan, A.P. McMahon and J. Motoyama for cDNA constructs. This work was supported by Advanced Brain Research grants from the Ministry of Education, Science, Sports, Culture, and Technology, and also partly by Health Sciences Research grants for Human Genome, Tissue Engineering, Food Biotechnology from the Ministry of Labor, Health, and Welfare.

References

[1] R.M. Abdel-Majid, W.L. Leong, L.C. Schalkwyk, D.S. Smallman, S.T. Wong, D.R. Storm, A. Fine, M.J. Dobson, D.L. Guernsey, P.E. Neumann, Loss of adenylyl cyclase I activity disrupts patterning of mouse somatosensory cortex, Nat. Genet. 19 (1998) 289–291.

[2] A. Agmon, L.T. Yang, E.G. Jones, D.K. O'Dowd, Topological precision in the thalamic projection to neonatal mouse barrel cortex, J. Neurosci. 15 (1995) 549–561.

[3] E. Ahissar, R. Sosnik, S. Haidarliu, Transformation from temporal to rate coding in a somatosensory thalamocortical pathway, Nature 406 (2000) 302–306.

[4] F.L. Andres, Supranumerary barrels develop in the somatosensory cortex of mice, after the implantation of the vibrissal follicle parts containing large numbers of receptors, J. Neural Transplant. 1 (1989) 33–47.

[5] F.L. Andres, H. van der Loos, Cultured embryonic non-innervated mouse muzzle is capable of generating a whisker pattern, Int. J. Dev. Neurosci. 1 (1983) 319–338.

[6] G.R. Belford, H.P. Killackey, The development of vibrissae representation in subcortical trigeminal centers of the neonatal rat, J. Comp. Neurol. 188 (1979) 63–74.

[7] K.M. Bishop, G. Goudreau, D.D. O'Leary, Regulation of area identity in the mammalian neocortex by Emx2 and Pax6, Science 288 (2000) 344–349.

[8] M. Blessing, L.B. Nanney, L.E. King, C.M. Jones, B.L. Hogan, Transgenic mice as a model to study the role of TGF-beta-related molecules in hair follicles, Genes Dev. 7 (1993) 204–215.

[9] C. Chiang, R.Z. Swan, M. Grachtchouk, M. Bolinger, Y. Litingtung, E.K. Robertson, M.K. Cooper, W. Gaffield, H. Westphal, P.A. Beachy, A.A. Dlugosz, Essential role for Sonic hedgehog during hair follicle morphogenesis, Dev. Biol. 205 (1999) 1–9.

[10] M. Cohen-Tannoudji, C. Babinet, M. Wassef, Early determination of a mouse somatosensory cortex marker, Nature 368 (1994) 460–463.

[11] M.C. Crair, D.C. Gillespie, M.P. Stryker, The role of visual experience in the development of columns in cat visual cortex, Science 279 (1998) 566–570.

[12] J.C. Crowley, L.C. Katz, Development of ocular dominance columns in the absence of retinal input, Nat. Neurosci. 2 (1999) 1125–1130.

[13] J.C. Crowley, L.C. Katz, Early development of ocular dominance columns, Science 290 (2000) 1321–1324.

[14] P. Davidson, M.H. Hardy, The development of mouse vibrissae in vivo and in vitro, J. Anat. 86 (1952) 342–356.

[15] D.R. Dawson, H.P. Killackey, Distinguishing topography and somatotopy in the thalamocortical projections of the developing rat, Brain Res. 349 (1985) 309–313.

[16] M.E. Dickinson, M.S. Kobrin, C.M. Silan, D.M. Kingsley, M.J. Justice, D.A. Miller, J.D. Ceci, L.F. Lock, A. Lee, A.M. Buchberg et al., Chromosomal localization of seven members of the murine TGF-beta superfamily suggests close linkage to several morphogenetic mutant loci, Genomics 6 (1990) 505–520.

[17] G. Drossopoulou, K.E. Lewis, J.J. Sanz-Ezquerro, N. Nikbakht, A.P. McMahon, C. Hofmann, C. Tickle, A model for anteroposterior patterning of the vertebrate limb based on sequential long- and short-range Shh signalling and Bmp signalling, Development 127 (2000) 1337–1348.

[18] R.S. Eruzurumlu, P.C. Kind, Neural activity: sculptor of 'barrels' in the neocortex, Trends Neurosci. 24 (2001) 589–595.

[19] K. Fox, B.L. Schlaggar, S. Glazewski, D.D. O'Leary, Glutamate receptor blockade at cortical synapses disrupts development of thalamocortical and columnar organization in somatosensory cortex, Proc. Natl. Acad. Sci. USA 93 (1996) 5584–5589.

[20] T. Fukuchi-Shimogori, E.A. Grove, Neocortex patterning by the secreted signaling molecule FGF8, Science 294 (2001) 1071–1074.

[21] A.J. Hannan, C. Blakemore, A. Katsnelson, T. Vitalis, K.M. Huber, M. Bear, J. Roder, D. Kim, H.S. Shin, P.C. Kind, PLC-beta1, activated via mGluRs, mediates activity-dependent differentiation in cerebral cortex, Nat. Neurosci. 4 (2001) 282–288.

[22] U. Heberlein, C.M. Singh, A.Y. Luk, T.J. Donohoe, Growth and differentiation in the Drosophila eye coordinated by hedgehog, Nature 373 (1995) 709–711.

[23] J.M. Hebert, T. Rosenquist, J. Gotz, G.R. Martin, FGF5 as a regulator of the hair growth cycle: evidence from targeted and spontaneous mutations, Cell 78 (1994) 1017–1025.

[24] J. Huelsken, R. Vogel, B. Erdmann, G. Cotsarelis, W. Birchmeier, beta-Catenin controls hair follicle morphogenesis and stem cell differentiation in the skin, Cell 105 (2001) 533–545.

[25] S. Iseki, A. Araga, H. Ohuchi, T. Nohno, H. Yoshioka, F. Hayashi, S. Noji, Sonic hedgehog is expressed in epithelial cells during development of whisker, hair, and tooth, Biochem. Biophys. Res. Commun. 218 (1996) 688–693.

[26] T. Iwasato, A. Datwani, A.M. Wolf, H. Nishiyama, Y. Taguchi, S. Tonegawa, T. Knopfel, R.S. Erzurumlu, S. Itohara, Cortex-restricted disruption of NMDAR1 impairs neuronal patterns in the barrel cortex, Nature 406 (2000) 726–731.

[27] C.M. Jones, K.M. Lyons, B.L. Hogan, Involvement of Bone Morphogenetic Protein-4 (BMP-4) and Vgr-1 in morphogenesis and neurogenesis in the mouse, Development 111 (1991) 531–542.

[28] H.P. Killackey, Pattern formation in the trigeminal system of the rat, Trends Neurosci. 3 (1980) 303–306.

[29] J. Kishimoto, R.E. Burgeson, B.A. Morgan, Wnt signaling maintains the hair-inducing activity of the dermal papilla, Genes Dev. 14 (2000) 1181–1185.

[30] R.O. Kuljis, P. Rakic, Hypercolumns in primate visual cortex can develop in the absence of cues from photoreceptors, Proc. Natl. Acad. Sci. USA 87 (1990) 5303–5306.

[31] E. Laufer, C.E. Nelson, R.L. Johnson, B.A. Morgan, C. Tabin, Sonic hedgehog and Fgf-4 act through a signaling cascade and feedback loop to integrate growth and patterning of the developing limb bud, Cell 79 (1994) 993–1003.

[32] A. Liu, A.L. Joyner, D.H. Turnbull, Alternation of limb and brain patterning in early mouse embryos by ultrasound-guided injection of Shh-expressing cells, Mech. Dev. 75 (1998) 107–115.

[33] K.M. Lyons, R.W. Pelton, B.L. Hogan, Patterns of expression of murine Vgr-1 and BMP-2a RNA suggest that transforming growth factor-beta-like genes coordinately regulate aspects of embryonic development, Genes Dev. 3 (1989) 1657–1668.
[34] C. Ma, Y. Zhou, P.A. Beachy, K. Moses, The segment polarity gene hedgehog is required for progression of the morphogenetic furrow in the developing Drosophila eye, Cell 75 (1993) 927–938.
[35] D.L. Maier, S. Mani, S.L. Donovan, D. Soppet, L. Tessarollo, J.S. McCasland, K.F. Meiri, Disrupted cortical map and absence of cortical barrels in growth-associated protein (GAP)-43 knockout mice, Proc. Natl. Acad. Sci. USA 96 (1999) 9397–9402.
[36] V. Marigo, M.P. Scott, R.L. Johnson, L.V. Goodrich, C.J. Tabin, Conservation in hedgehog signaling: induction of a chicken patched homolog by Sonic hedgehog in the developing limb, Development 122 (1996) 1225–1233.
[37] E. Marti, D.A. Bumcrot, R. Takada, A.P. McMahon, Requirement of 19K form of Sonic hedgehog for induction of distinct ventral cell types in CNS explants, Nature 375 (1995) 322–325.
[38] S. Miyake, M. Makimura, Y. Kanegae, S. Harada, Y. Sato, K. Takamori, C. Tokuda, I. Saito, Efficient generation of recombinant adenoviruses using adenovirus DNA–terminal protein complex and a cosmid bearing the full-length virus genome, Proc. Natl. Acad. Sci. USA 93 (1996) 1320–1324.
[39] E.M. Miyashita-Lin, R. Hevner, K.M. Wassarman, S. Martinez, J.L. Rubenstein, Early neocortical regionalization in the absence of thalamic innervation, Science 285 (1999) 906–909.
[40] B.A. Morgan, R.W. Orkin, S. Noramly, A. Perez, Stage-specific effects of sonic hedgehog expression in the epidermis, Dev. Biol. 201 (1998) 1–12.
[41] J. Motoyama, H. Heng, M.A. Crackower, T. Takabatake, K. Takeshima, L.C. Tsui, C. Hui, Overlapping and non-overlapping Ptch2 expression with Shh during mouse embryogenesis, Mech. Dev. 78 (1998) 81–84.
[42] J. Motoyama, T. Takabatake, K. Takeshima, C. Hui, Ptch2, a second mouse Patched gene is co-expressed with Sonic hedgehog, Nat. Genet. 18 (1998) 104–106.
[43] C.J. Neumann, C. Nuesslein-Volhard, Patterning of the zebrafish retina by a wave of sonic hedgehog activity, Science 289 (2000) 2137–2139.
[44] J.C. Nussbaumer, H. Van der Loos, An electrophysiological and anatomical study of projections to the mouse cortical barrelfield and its surroundings, J. Neurophysiol. 86 (1985) 686–698.
[45] K. Ohsaki, T. Morimitsu, Y. Ishida, R. Kominami, N. Takahashi, Expression of the Vax family homeobox genes suggests multiple roles in eye development, Genes Cells 4 (1999) 267–276.
[46] A. Orr-Urtreger, D. Givol, A. Yayon, Y. Yarden, P. Lonai, Developmental expression of two murine fibroblast growth factor receptors, flg and bek, Development 113 (1991) 1419–1434.
[47] M.C. Osterheld-Haas, J.P. Hornung, Laminar development of the mouse barrel cortex: effects of neurotoxins against monoamines, Exp. Brain Res. 110 (1996) 183–195.
[48] K.G. Peters, S. Werner, G. Chen, L.T. Williams, Two FGF receptor genes are differentially expressed in epithelial and mesenchymal tissues during limb formation and organogenesis in the mouse, Development 114 (1992) 233–243.
[49] B. Pidoux, R. Verley, E. Farkas, J. Scherrer, Projections of the common fur of the muzzle upon the cortical area for mystacial vibrissae in rats dewhiskered since birth, Neurosci. Lett. 11 (1979) 301–306.
[50] K.A. Platt, J. Michaud, A.L. Joyner, Expression of the mouse Gli and Ptc genes is adjacent to embryonic sources of hedgehog signals suggesting a conservation of pathways between flies and mice, Mech. Dev. 62 (1997) 121–135.
[51] N. Prakash, P. Vanderhaeghen, S. Cohen-Cory, J. Frisen, J.G. Flanagan, R,D. Frostig, Malformation of the functional organization of somatosensory cortex in adult Ephrin-A5 knock-out mice revealed by in vivo functional imaging, J. Neurosci. 20 (2000) 5841–5847.
[52] S. Reddy, T. Andl, A. Bagasra, M.M. Lu, D.J. Epstein, E.E. Morrisey, S.E. Millar, Characterization of Wnt gene expression in developing and postnatal hair follicles and identification of Wnt5a as a target of Sonic hedgehog in hair follicle morphogenesis, Mech. Dev. 107 (2001) 69–82.
[53] A.W. Roe, S.L. Pallas, J.O. Hahm, M. Sur, A map of visual space induced in primary auditory cortex, Science 250 (1990) 818–820.
[54] H. Roelink, J.A. Porter, C. Chiang, Y. Tanabe, D.T. Chang, P.A. Beachy, T.M. Jessell, Floor plate and motor neuron induction by different concentrations of the amino-terminal cleavage product of sonic hedgehog autoproteolysis, Cell 81 (1995) 445–455.
[55] T.A. Rosenquist, G.R. Martin, Fibroblast growth factor signalling in the hair growth cycle: expression of the fibroblast growth factor receptor and ligand genes in the murine hair follicle, Dev. Dyn. 205 (1996) 379–386.
[56] B.L. Schlaggar, K. Fox, D.D. O'Leary, Postsynaptic control of plasticity in developing somatosensory cortex, Nature 364 (1993) 623–626.
[57] J. Sharma, A. Angelucci, M. Sur, Induction of visual orientation modules in auditory cortex, Nature 404 (2000) 841–847.
[58] B. St-Jacques, H.R. Dassule, I. Karavanova, V.A. Botchkarev, J. Li, P.S. Danielian, J.A. McMahon, P.M. Lewis, R. Paus, A.P. McMahon, Sonic hedgehog signaling is essential for hair development, Curr. Biol. 8 (1998) 1058–1068.
[59] R.N. Strominger, T.A. Woolsey, Templates for locating the whisker area in fresh flattened mouse and rat cortex, J. Neurosci. Methods 22 (1987) 113–118.
[60] S. Tanaka, Experience-dependent self-organization of biological neural networks, NEC Res. Dev. 98 (1990) 1–14.
[61] P. Vanderhaeghen, Q. Lu, N. Prakash, J. Frisen, C.A. Walsh, R.D. Frosting, J.G. Flanagan, A mapping label required for normal scale of body representation in the cortex, Nat. Neurosci. 3 (2000) 358–365.
[62] H. Van der Loos, J. Dorfl, E. Welker, Variation in pattern of mystacial vibrissae in mice. A quantitative study of ICR stock and several inbred strains, J. Hered. 75 (1984) 326–336.
[63] H. Van der Loos, T.A. Woolsey, Somatosensory cortex: structural alterations following early injury to sense organs, Science 179 (1973) 395–398.
[64] C. van Genderen, R.M. Okamura, I. Farinas, R.G. Quo, T.G. Parslow, L. Bruhn, R. Grosschedl, Development of several organs that require inductive epithelial–mesenchymal interactions is impaired in LEF-1-deficient mice, Genes Dev. 8 (1994) 2691–2703.
[65] P.M. Waite, L.R. Marotte, C.A. Leamey, R.F. Mark, Development of whisker-related patterns in marsupials: factors controlling timing, Trends Neurosci. 21 (1998) 265–269.
[66] E. Welker, M. Armstrong-James, G. Bronchti, W. Ourednik, F. Gheorghita-Baechler, R. Dubois, D.L. Guernsey, H. van der Loos, P.E. Neumann, Altered sensory processing in the somatosensory cortex of the mouse mutant barrelless, Science 271 (1996) 1864–1867.
[67] T.A. Woolsey (Ed.), Structural, Functional and Biochemical Plasticity in the Rodent Brain, Pontifica Academia Scientiarum, Vatican City, 1987, pp. 347–380.
[68] M. Yamakado, T. Yohro, Subdivision of mouse vibrissae on an embryological basis, with descriptions of variations in the number and arrangement of sinus hairs and cortical barrels in BALB/c (nu/+; nude, nu/nu) and hairless (hr/hr) strains, Am. J. Anat. 155 (1979) 153–174.
[69] P. Zhou, C. Byrne, J. Jacobs, E. Fuchs, Lymphoid enhancer factor 1 directs hair follicle patterning and epithelial cell fate, Genes Dev. 9 (1995) 700–713.

Dominant-negative inhibition of prion replication in transgenic mice

Véronique Perrier*†, Kiyotoshi Kaneko*‡, Jiri Safar*, Julie Vergara*, Patrick Tremblay*§, Stephen J. DeArmond*¶, Fred E. Cohen*‖**††, Stanley B. Prusiner*‖‡‡§§, and Andrew C. Wallace**¶¶

*Institute for Neurodegenerative Diseases and Departments of ¶Pathology, ‖Biochemistry and Biophysics, **Cellular and Molecular Pharmacology, ††Medicine, and ‡‡Neurology, University of California, San Francisco, CA 94143-0518

Contributed by Stanley B. Prusiner, July 17, 2002

Our discovery of dominant-negative inhibition of prion formation in cultured cells provided an explanation for the resistance of some sheep to scrapie and humans to Creutzfeldt–Jakob disease. To determine whether dominant-negative inhibition occurs *in vivo*, we produced transgenic (Tg) mice expressing prion protein (PrP) with either the Q167R or Q218K mutation alone or in combination with wild-type (wt) PrP. Tg(MoPrP,Q167R)*Prnp*$^{0/0}$ mice expressing mutant PrP at levels equal to non-Tg mice remained healthy for >550 days, indicating that inoculation with prions did not cause disease. Immunoblots of brain homogenates and histologic analysis did not reveal abnormalities. Tg(MoPrP,Q167R)*Prnp*$^{+/+}$ mice expressing both mutant and wt PrP did not exhibit neurologic dysfunction, but their brains revealed low levels of the PrP pathogenic isoform (PrP^{Sc}), and sections showed numerous vacuoles and severe astrocytic gliosis at 300 days after inoculation. Both Tg(MoPrP,Q218K)*Prnp*$^{0/0}$ and Tg(MoPrP,Q218K)*Prnp*$^{+/+}$ mice expressing high levels of the transgene product remained healthy for >300 days after inoculation. Neither PrP^{Sc} nor neuropathologic changes were found. Our studies demonstrate that although dominant-negative inhibition of wt PrP^{Sc} formation occurs, expression of the dominant-negative PrP at the same level as wt PrP does not prevent prion formation completely. However, expression of dominant-negative PrP alone had no deleterious effects on the mice and did not support prion propagation.

In prion diseases, the aberrantly folded isoform (PrP^{Sc}) of the normal, cellular prion protein (PrP^{C}) stimulates the conversion of PrP^{C} into nascent PrP^{Sc}. The accumulation of PrP^{Sc} leads to CNS dysfunction and neuronal degeneration (1). At present, there is no accepted therapy for prion diseases, and whether the drug quinacrine will prove to be effective in treating these diseases remains to be established (2). In addition to quinacrine (3), other compounds that block prion replication as well as stimulate the clearance of existing prions include branched polyamines (4), phthalocyanines and porphyrin derivatives (5), Congo red (6), compound 60 (7), β-breaker peptides (8), and anti-PrP antibodies (9, 10). Although many of the foregoing compounds are able to clear prions in scrapie-infected neuroblastoma cells, none have been shown to be effective in animals or humans to date (11). It is noteworthy that both vaccination and passive immunization have effectively decreased Aβ amyloid deposits in the brains of transgenic (Tg) mice expressing mutant amyloid precursor protein (12–14). Unfortunately, some attempts to vaccinate humans with Aβ have resulted in an allergic meningoencephalitis, which halted a clinical trial (15).

One compound noted above was designed to mimic dominant-negative inhibition of prion replication (7). Dominant-negative inhibition occurs when the product of the mutant or variant allele interferes with a function of the wild-type (wt) allelic protein. Naturally occurring polymorphic variants of PrP, Q171R and E219K, known to render sheep and humans resistant to scrapie and Creutzfeldt–Jakob disease, respectively (16–18), were found to act as dominant negatives in scrapie-infected neuroblastoma cells (19, 20).

Based on these findings, we undertook studies on dominant-negative PrP. Tg mice expressing mutant PrP with either Q167R or Q218K or coexpressing mutant and wt PrP were inoculated with Rocky Mountain Laboratory (RML) prions, and incubation times were determined. We found that expression of dominant-negative PrP at the same level as wt PrP dramatically slowed PrP^{Sc} formation. Moreover, dominant-negative PrP was not converted into PrP^{Sc}, and its expression, even at high levels, had no deleterious effects on the mice.

Materials and Methods

Nomenclature. Residue 171 in sheep PrP corresponds to codon 167 in mouse PrP (MoPrP) and codon 168 in human PrP (HuPrP). Residue 219 in HuPrP corresponds to codon 218 in MoPrP.

Laboratory Animals and Inoculum. We obtained wt FVB mice from Charles River Breeding Laboratories. Tg(MoPrP-A)4053 mice have been described (21). MoPrP,Q167R and MoPrP,Q218K mutant genes were subcloned into the cosTet vector for microinjection (19). Tg(MoPrP,Q167R)*Prnp*$^{0/0}$ and Tg(MoPrP,Q218K)*Prnp*$^{0/0}$ founder mice were identified by PCR screening for transgene integration by using a Beckman robotic workstation.

Tg(MoPrP,Q167R)*Prnp*$^{+/+}$ and Tg(MoPrP,Q218K)*Prnp*$^{+/+}$ mice were produced by repeated back-crossing of Tg(MoPrP,Q167R)*Prnp*$^{0/0}$ and Tg(MoPrP,Q218K)*Prnp*$^{0/0}$ mice, respectively, with FVB mice until we obtained the third (F_3) generation. In these mice, both the transgene and wt *Prnp* genes were identified by PCR screening.

The RML prion inoculum was as described (22).

Determination of Incubation Periods. Control and Tg mice were inoculated intracerebrally with 30 μl of a 1% RML preparation or 10% brain homogenate prepared in PBS. Beginning 50 days after inoculation, the mice were monitored daily, and the neurologic status was assessed semiweekly as described (23). Mice scored positively for prion disease when two or three signs of neurologic dysfunction were present and progressive deterioration was apparent according to 16 diagnostic criteria as described (24, 25).

Antibodies. Two chimeric human–mouse (HuM) recombinant antibody fragments (recFab), D13 and R1, that recognize PrP(97–106) and PrP(225–231), respectively, were used for immunoblot analysis (9, 26).

Preparation of Brain Homogenates and Immunoblot Analysis. We prepared 10% brain homogenates in PBS by using a 5-ml syringe

Abbreviations: PrP, prion protein; PrP^{Sc}, PrP pathogenic isoform; PrP^{C}, PrP normal cellular isoform; Tg, transgenic; wt, wild type; RML, Rocky Mountain Laboratory; MoPrP, mouse PrP; HuPrP, human PrP; HuM, human–mouse; PK, proteinase K; CDI, conformation-dependent immunoassay; N, native; D, denatured.

†Present address: Institut de Génétique Humaine, Montpellier Cedex 5, France.

‡Present address: National Center of Neurology and Psychiatry, Kodaira, Tokyo 187-8502, Japan.

§Present address: Neurochem, Inc., Ville St. Laurent, QC, Canada H4S 2A1.

§§To whom reprint requests should be addressed at: Institute for Neurodegenerative Diseases, University of California, Box 0518, San Francisco, CA 94143-0518.

¶¶Present address: Structural GenomiX, San Diego, CA 92121.

Table 1. Susceptibility of Tg(MoPrP,Q167R) mice to RML prions

Host	PrP expression level* Mutant	wt	Inoculum	Incubation period, days ± SEM	n/n_0†
FVB	0	1×	RML	127 ± 1	50/50
Tg(MoPrP,Q167R)*Prnp*$^{0/0}$	1×	0	RML	>550	0/8
Tg(MoPrP,Q167R)*Prnp*$^{0/0}$	1×	0	RML	>557	0/4
Tg(MoPrP,Q167R)*Prnp*$^{0/0}$	1×	0	None	>557	0/10
FVB/*Prnp*$^{0/0}$	0	0	RML	>557	0/7
Tg(MoPrP,Q167R)*Prnp*$^{+/+}$	1×	1×	RML	447 ± 11	7/10‡
Tg(MoPrP,Q167R)*Prnp*$^{+/+}$	1×	1×	None	>256	0/6

*Expression levels were determined by comparing serial dilutions of Tg mouse brain homogenates to that of normal FVB mice (1 × PrP level) by immunoblot.

†n, number of sick mice; n_0, number of inoculated mice.

‡Seven animals died atypically of prolapsus at the mean incubation time indicated; three healthy animals were killed at 300 days for Western blot and histoblot analyses.

coupled to gauge needles of decreasing diameters and by repeated suctions and extrusions of the solution. After the solution was centrifuged for 5 min at 2,000 rpm in a Beckman centrifuge, the supernatant was collected. Protein concentration was measured with the bicinchoninic acid reagent (BCA, Pierce) and corresponds to 10 mg/ml. Volumes (500 μl) of 1% homogenates were prepared in PBS and 2% Sarkosyl and digested with 20 μg/ml of proteinase K (PK) at a ratio of 1:50 (PK/protein) for 1 h at 37°C. The digestion was stopped with 5 mM phenylmethylsulfonyl fluoride. PK-treated samples were mixed with an equal volume of SDS-loading buffer and boiled for 5 min, and 30 μl were loaded on 12% SDS/PAGE precast gels (Bio-Rad). Undigested samples were prepared by mixing an aliquot of 10% homogenate with an equal volume of SDS-loading buffer and then boiled for 5 min. Prepared samples (10 μl) were loaded on 12% SDS/PAGE precast gels. Immunoblot analysis was performed according to a protocol described previously (28).

Quantification of PrP^{Sc} by Conformation-Dependent Immunoassay (CDI). To detect levels of PrP^{Sc}, an immunoassay was performed on Syrian hamster PrP according to a technique described previously (29).

Preparation of the Calibration Curve. Brains from normal or RML-inoculated FVB mice were resuspended to 5% solution, in PBS and 2% Sarkosyl, as described above. Fivefold serial dilutions were performed by diluting the 5% RML-FVB brain homogenate with 5% normal FVB brain homogenate. Ten-point dilutions were completed starting at 1% and continuing with 0.2, 0.04, 0.008%, etc. Then, 1-ml aliquots were digested with 25 μg/ml PK at a 1:200 ratio (PK/protein) for 1 h at 37°C on a shaker. The reaction was stopped by a mixture of protease inhibitors; samples were precipitated with sodium phosphotungstate and processed as described in ref. 29. The samples were quantified by CDI using time-resolved fluorescence spectroscopy (29). The europium-labeled HuM-D13 Fab was used to detect mutant and wt MoPrP.

Preparation of Modified MoPrP. The 10% brain homogenates previously analyzed by immunoblots were tested also by CDI. Homogenates were diluted to 5% solution in PBS/2% Sarkosyl and rehomogenized with a syringe to break aggregates. Aliquots of 1 ml were digested with 25 μg/ml PK for 1 h at 37°C on a shaker. The samples were processed as described above.

Neuropathology. Brain tissue was immersion-fixed in 10% buffered formalin immediately after the mice were killed. Histological sections were prepared and stained with hematoxylin/eosin as described (30).

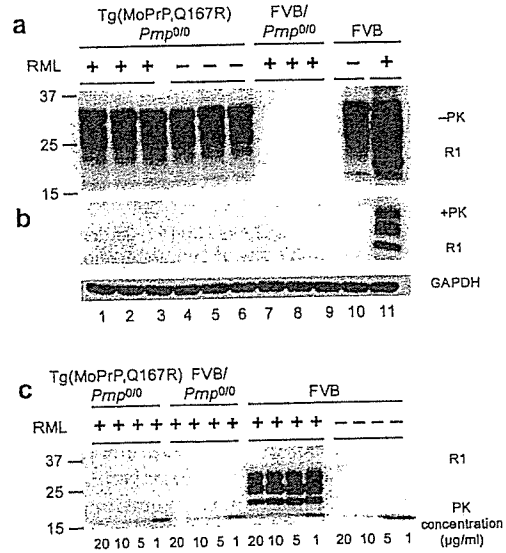

Fig. 1. Immunoblots of Tg(MoPrP,Q167R)*Prnp*$^{0/0}$ mice. (*a* and *b*) Brain homogenates were analyzed before (*a*) and after (*b*) PK digestion. The plus (+) and minus (−) signs indicate that the mice were and were not inoculated, respectively, with RML prions. Lanes 1–6, six independent Tg(MoPrP,Q167R)*Prnp*$^{0/0}$ mice killed after 550 (lanes 1–3) and 420 (lanes 4–6) days; lanes 7–9, three FVB/*Prnp*$^{0/0}$ mice killed after 420 days; lane 10, normal, wt FVB mouse; lane 11, wt FVB mouse inoculated with prions and sick after ≈120 days. (*a*) In each lane, 50 μg of 10% brain homogenate was loaded. GAPDH, glyceraldehyde 3-phosphate dehydrogenase. (*c*) PK digestion of brain homogenates from Tg(MoPrP,Q167R)*Prnp*$^{0/0}$ and wt FVB mice. The PK concentrations used are indicated. All membranes were probed with HuM-R1 Fab at a final concentration of 1 μg/ml. A secondary antibody coupled with horseradish peroxidase was also diluted to a final concentration of 1 μg/ml. Blots were developed with the enhanced chemiluminescence (ECL) kit (Amersham Pharmacia). The numbers to the left of each blot indicate the molecular mass of protein standards in kDa.

Histoblots. Histoblots were performed as described in ref. 31.

Results

RML Prions in Tg(MoPrP,Q167R) Mice. To study the effect of Q167R on prion formation, we constructed Tg mice expressing mutated MoPrP(Q167R) on the PrP-deficient (*Prnp*$^{0/0}$) background. These mice, designated Tg(MoPrP,Q167R)*Prnp*$^{0/0}$, express PrP at the same levels as FVB mice and were inoculated with RML prions. None of the 12 inoculated mice showed signs of disease after 550 days (Table 1). Uninoculated Tg(MoPrP,Q167R)*Prnp*$^{0/0}$ mice showed no signs of spontaneous neurodegeneration. FVB control mice developed signs of CNS dysfunction at 127 ± 1 days after inoculation. *Prnp*$^{0/0}$ mice inoculated with RML prions did not show signs of disease after >550 days (Table 1).

Tg(MoPrP,Q167R)*Prnp*$^{+/+}$ mice express the same levels of both wt $MoPrP^C$ and mutant MoPrP(Q167R). Seven of the 10 Tg(MoPrP,Q167R)*Prnp*$^{+/+}$ mice showed signs of CNS dysfunction at more than 400 days after inoculation with prions.

Immunoblot Analysis of Tg(MoPrP,Q167R) Mice. Tg(MoPrP,Q167R)-*Prnp*$^{0/0}$ mice that remained healthy were killed for immunoblot analysis to determine the level of PrP transgene expression (Fig. 1*a*). Equal amounts of protein were loaded on the gel as judged by immunoblotting of glyceraldehyde 3-phosphate dehydrogenase.

Brain homogenates from FVB mice inoculated with RML prions were subjected to limited proteolysis; these samples gave a strong protease-resistant PrP^{Sc} signal (Fig. 1*b*, lane 11). PK-digested samples from inoculated Tg(MoPrP,Q167R)*Prnp*$^{0/0}$ (Fig. 1*b*, lanes

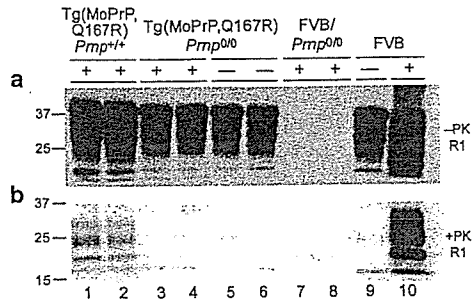

Fig. 2. Immunoblots of Tg(MoPrP,Q167R) mice. (*a* and *b*) Brain homogenates were analyzed by immunoblot before (*a*) and after (*b*) PK digestion. The plus (+) and minus (−) signs indicate that the mice were and were not inoculated, respectively, with RML prions. Lanes 1 and 2, two independent Tg(MoPrP,Q167R)*Prnp*$^{+/+}$ mice killed after 300 days; lanes 3–6, Tg(MoPrP,Q167R)*Prnp*$^{0/0}$ mice killed after 550 (lanes 3 and 4) and 420 (lanes 5 and 6) days; lanes 7 and 8, FVB/*Prnp*$^{0/0}$ mice killed after 420 days; lane 9, normal, wt FVB mouse; lane 10, wt FVB mouse that became ill after ≈120 days. Membranes were probed with HuM-R1 Fab at a final concentration of 1 μg/ml.

1–3), uninoculated Tg(MoPrP,Q167R)*Prnp*$^{0/0}$ (Fig. 1*b*, lanes 4–6), inoculated *Prnp*$^{0/0}$ (Fig. 1*b*, lanes 7–9), and uninoculated FVB mice (Fig. 1*b*, lane 10) showed no detectable PrP^{Sc}. Prolonged exposure of the film, up to 15 min, did not reveal a PrP^{Sc} signal. A second Western blot was probed with HuM-D13 Fab and showed no PrP^{Sc} in Tg(MoPrP,Q167R)*Prnp*$^{0/0}$ mice inoculated with prions (data not shown).

Because the Q167R mutation might render PrP^{Sc} more sensitive to PK-catalyzed hydrolysis, we digested the samples with PK concentrations ranging from 1 to 20 μg/ml (Fig. 1*c*). Brains from FVB mice inoculated with RML prions showed an increased PrP^{Sc} signal with lower PK concentrations; however, no PrP^{Sc} band was present in the brain extracts of both inoculated and uninoculated Tg(MoPrP,Q167R)*Prnp*$^{0/0}$ mice even at 1 μg/ml PK. Based on these immunoblots and the lack of neuropathology in Tg(MoPrP,Q167R)*Prnp*$^{0/0}$ mice, we conclude that MoPrP(Q167R) is unable to support PrP^{Sc} formation.

None of the 10 Tg(MoPrP,Q167R)*Prnp*$^{+/+}$ mice, which express same levels of both wt and mutant MoPrP, showed signs of CNS dysfunction more than 400 days after inoculation with prions (Table 1). To determine whether wt MoPrP^{C} in Tg(MoPrP,Q167R)-*Prnp*$^{+/+}$ mice supported prion replication, we killed two apparently healthy Tg(MoPrP,Q167R)*Prnp*$^{+/+}$ mice 300 days after inoculation and performed immunoblot analysis (Fig. 2). PK-digested homogenates revealed the presence of low amounts of protease-resistant PrP, with similar intensity (Fig. 2*b*, lanes 1 and 2). The intensity of these bands corresponds to ≈10% of the signal obtained with FVB mice inoculated with prions (Fig. 2*b*, lane 10), arguing for a diminished rate of PrP^{Sc} formation. The remaining seven inoculated Tg(MoPrP,Q167R)*Prnp*$^{+/+}$ mice presented atypical neurologic signs with a mean incubation time of 447 ± 11 days. Because we detected some wt PrP^{Sc} replication in the brains of these mice at 300 days, it seems likely that further prion replication occurred over the subsequent 150 days. The additional presumed replication of prions and neuropathology described below argue that these mice died of prion disease, but the cause of death remains to be established.

Neuropathology of Tg(MoPrP,Q167R) Mice. Pathological studies were performed on the midbrains of the Tg(MoPrP,Q167R) mice analyzed by immunoblotting (Figs. 1 and 2). Both inoculated and uninoculated Tg(MoPrP,Q167R)*Prnp*$^{0/0}$ mice showed no vacuolation in the hippocampus (Fig. 5 *e* and *g*, which is published as supporting information on the PNAS web site, www.pnas.org) but showed minimal astrocytic gliosis, which is consistent with aging (compare with Fig. 5 *f* and *h*).

In contrast, hippocampal sections from Tg(MoPrP,Q167R)-*Prnp*$^{+/+}$ mice revealed widespread vacuolation associated with severe astrocytic gliosis at 300 days after inoculation (Fig. 5 *i* and *j*). The severity of the neuropathologic changes resembled that of prion-inoculated FVB mice (Fig. 5 *a* and *b*). However, neurodegeneration was localized in the ventral hippocampus in Tg(MoPrP,Q167R)*Prnp*$^{+/+}$ mice, whereas both the ventral and dorsal hippocampus of FVB mice were affected, with the most intense changes in the dorsal area. Histopathologic analyses of uninoculated Tg(MoPrP,Q167R)*Prnp*$^{+/+}$ mice (Fig. 5 *k* and *l*) resembled those of uninoculated FVB mice (Fig. 5 *c* and *d*). Our findings show an excellent correlation between Western blot and neuropathological analysis; the presence of PrP^{Sc} was accompanied by vacuolation and astrocytic gliosis.

Localization of PrP^{Sc} in the Brains of Tg(MoPrP,Q167R) Mice. Histoblotting demonstrated widespread intense staining of the brains of RML-inoculated FVB mice with clinical signs of neurologic dysfunction (Fig. 6*a*, which is published as supporting information on the PNAS web site). Histoblots of the brains of Tg(MoPrP, Q167R)*Prnp*$^{0/0}$ mice inoculated with prions (Fig. 6*b*) were indistinguishable from uninoculated controls (Fig. 6*c*) and inoculated FVB/*Prnp*$^{0/0}$ mice (Fig. 6*d*). Minimal PrP^{Sc} deposits, localized primarily to the ventral hippocampus, were found in the brains of inoculated Tg(MoPrP,Q167R)*Prnp*$^{+/+}$ mice (Fig. 6*e*).

CDI of Tg(MoPrP,Q167R) Brain Homogenates. To quantify the PrP^{Sc} detected in Western blots, we used the CDI to measure both protease-resistant and protease-sensitive PrP^{Sc} (29). The CDI uses time-resolved fluorescence to measure the binding of antibodies to PrP before and after denaturation. The epitope for antibody binding is typically exposed in native (N) PrP^{C}, denatured (D) PrP^{C}, and denatured PrP^{Sc} but buried in native, infectious PrP^{Sc}. To establish a calibration curve for MoPrP^{Sc}, brain homogenates were prepared from FVB mice infected with RML prions (Fig. 3*a*). A linear relationship between PrP^{Sc} level and a brain dilution up to 3.2×10^{-5} was demonstrated. Whether MoPrP^{Sc} was detected after a dilution of 10^{-6}, which corresponds to a D/N ratio of 1.25 ± 0.04, is unclear. Control brain homogenates from uninoculated FVB mice gave a D/N ratio of 1.1 ± 0.04 (Fig. 3*b*) in contrast to a value of 1.67 for Syrian hamster brains (29).

Brain homogenates (1%, wt/vol) prepared from RML-inoculated FVB mice gave a D/N ratio of 82 ± 2.3. We prepared 5% brain homogenates from Tg mice to detect potential traces of PrP^{Sc}. Using the CDI, we detected PrP^{Sc} only in homogenates from RML-inoculated Tg(MoPrP,Q167R)*Prnp*$^{+/+}$ mice, with samples from two animals giving D/N ratios of 46 ± 1.5 and 45 ± 1.6 (Fig. 3*b*), which correspond to 0.05 μg/ml PrP^{Sc}. These D/N values for Tg(MoPrP,Q167R)*Prnp*$^{+/+}$ mice were measured in homogenates that were five times more concentrated than those from FVB mice, therefore equivalent 1% homogenates would give values of 9.2 ± 0.3 and 9.0 ± 0.32. Comparing D/N values, we have ≈9 times less PrP^{Sc} in Tg(MoPrP,Q167R)*Prnp*$^{+/+}$ than in normal FVB mice, a finding that correlates with Western blot analysis (Fig. 2*b*, lanes 1 and 2) and histoblots (Fig. 6*e*). In contrast, uninoculated Tg(MoPrP,Q167R)*Prnp*$^{+/+}$ mice as well as inoculated Tg(MoPrP,Q167R)*Prnp*$^{0/0}$ and *Prnp*$^{0/0}$ mice gave D/N ratios between 0.58 ± 0.04 and 1.2 ± 0.01, indicating the absence of PrP^{Sc}.

RML Prions in Tg(MoPrP,Q218K) Mice. Because dominant-negative inhibition of prion replication in Tg(MoPrP,Q167R)*Prnp*$^{+/+}$ mice was incomplete, we produced mice expressing high levels of MoPrP(Q218K). Two lines were established, Tg(MoPrP,Q218K)-22500/*Prnp*$^{0/0}$ and Tg(MoPrP,Q218K)21603/*Prnp*$^{0/0}$, that express mutant PrP at levels 32 and 16 times that of FVB mice, respectively. Additionally, we produced Tg(MoPrP,Q218K)22500/*Prnp*$^{+/+}$ and

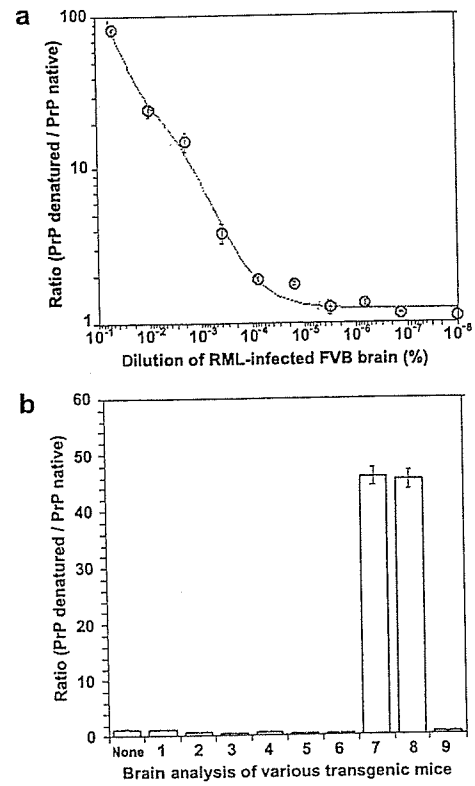

Fig. 3. CDI analysis of Tg(MoPrP,Q167R) mice. (*a*) Calibration curve performed on brain extracts of inoculated FVB mice. The europium-labeled HuM-D13 Fab was used for the detection of PrP. (*b*) CDI analysis of various brain homogenates. None, uninoculated wt FVB mice; 1 and 2, two prion-inoculated Tg(MoPrP,Q167R)*Prnp*$^{0/0}$ mice killed after 550 days; 3 and 4, two uninoculated Tg(MoPrP,Q167R)*Prnp*$^{0/0}$ mice killed after 420 days; 5 and 6, prion-inoculated FVB/*Prnp*$^{0/0}$ mice killed after 420 days; 7 and 8, prion-inoculated Tg(MoPrP,Q167R)*Prnp*$^{+/+}$ mice killed after 300 days; 9, an uninoculated Tg(MoPrP,Q167R)*Prnp*$^{+/+}$ mouse killed after 150 days. Data points and bars are average ± SEM obtained from three independent measurements.

Tg(MoPrP,Q218K)21603/*Prnp*$^{+/+}$ mice, which overexpress mutant PrP and express wt PrP at 1× level. We inoculated these mice with RML prions.

Of 16 inoculated Tg(MoPrP,Q218K)22500/*Prnp*$^{0/0}$ mice, 12 showed signs of disease with a mean incubation time of 476 ± 31 days. It is likely that these animals developed a spontaneous disease because 6 of 10 uninoculated mice also died with a mean survival time of 442 ± 49 days (Table 2). This result is not surprising because of the high expression level (32×) of the transgene; high levels of PrP expression have been reported to cause disease (32).

Similar results were obtained with Tg(MoPrP,Q218K)20250/*Prnp*$^{0/0}$ mice, which express mutant PrP at 32× level. All inoculated mice developed CNS dysfunction after 315 ± 33 days, whereas uninoculated mice showed clinical signs after 322 ± 30 days. Neuropathological examination revealed numerous vacuoles and pronounced astrocytic gliosis in both inoculated and uninoculated animals, and neither group had PrP^{Sc} based on immunoblots (data not shown). These findings argue that Tg(MoPrP,Q218K)22500/*Prnp*$^{0/0}$ mice develop spontaneous neurologic disease but are resistant to infection by RML prions.

Five of eight Tg(MoPrP,Q218K)22500/*Prnp*$^{+/+}$ mice inoculated with prions became ill, with a mean incubation time of 374 ± 24 days. It is possible that these mice also developed spontaneous neurodegeneration because noninoculated controls became ill, with one animal dying at 319 days and two mice still living but presenting signs of ataxia at 370 days (Table 2).

In contrast, Tg(MoPrP,Q218K)21603/*Prnp*$^{0/0}$ mice that express lower levels of PrP did not develop spontaneous disease. None of the 18 inoculated Tg(MoPrP,Q218K)21603/*Prnp*$^{0/0}$ mice showed signs of disease after more than 468 and 550 days, which is remarkable because of the 16× expression level. Five of nine Tg(MoPrP,Q218K)21603/*Prnp*$^{+/+}$ mice inoculated with prions developed disease with a mean incubation time of 412 ± 18 days. By comparison with Tg(MoPrP-A)4053 mice, Tg(MoPrP,Q218K)-21603/*Prnp*$^{+/+}$ mice exhibited a prolonged incubation time by a factor of approximately 8. Tg(MoPrP-A)4053 mice, expressing wt PrP at 8×, developed disease at 50 days after inoculation with RML prions (Table 2). Currently, two Tg(MoPrP,Q218K)21603/*Prnp*$^{+/+}$ mice remain healthy after 508 days, as is true for all uninoculated mice from this Tg line (Table 2).

Immunoblots of Tg(MoPrP,Q218K) Mice. To distinguish between neurodegeneration caused by prions and that caused by misprocessing of the transgene product, we performed immunoblotting on brain homogenates of Tg(MoPrP,Q218K)22500/*Prnp*$^{0/0}$ and Tg(MoPrP,Q218K)21603/*Prnp*$^{0/0}$ mice. We were interested in whether Tg(MoPrP,Q218K)22500/*Prnp*$^{+/+}$ and Tg(MoPrP,Q218K)21603/*Prnp*$^{+/+}$ mice were able to form nascent wt PrP^{Sc} as seen in Tg(MoPrP,Q167R)*Prnp*$^{+/+}$ mice. For each experimental group in Table 2, two animals were killed when they were young, and immunoblots were performed on their brain homogenates

Table 2. Susceptibility of Tg(MoPrP,Q218K) mice to RML prions

Host	PrP expression level*		Inoculum	Incubation period, days ± SEM	n/n_0†
	Mutant	wt			
Tg(MoPrP-A)4053/*Prnp*$^{0/0}$	0	8×	RML	50 ± 2	16/16
FVB/*Prnp*$^{0/0}$	0	0	RML	>550	0/6
Tg(MoPrP,Q218K)22500/*Prnp*$^{0/0}$	32×	0	RML	476 ± 31	12/16
Tg(MoPrP,Q218K)22500/*Prnp*$^{0/0}$	32×	0	None	442 ± 49	6/10
Tg(MoPrP,Q218K)22500/*Prnp*$^{+/+}$	32×	1×	RML	374 ± 24	5/8
Tg(MoPrP,Q218K)22500/*Prnp*$^{+/+}$	32×	1×	None	>376	1/6‡
Tg(MoPrP,Q218K)21603/*Prnp*$^{0/0}$	16×	0	RML	>550	0/8
Tg(MoPrP,Q218K)21603/*Prnp*$^{0/0}$	16×	0	RML	>468	0/10
Tg(MoPrP,Q218K)21603/*Prnp*$^{0/0}$	16×	0	None	>481	0/10
Tg(MoPrP,Q218K)21603/*Prnp*$^{+/+}$	16×	1×	RML	>508	5/9§
Tg(MoPrP,Q218K)21603/*Prnp*$^{+/+}$	16×	1×	None	>438	0/10

*Expression levels were determined as described for Table 1.
†n, number of sick mice; n_0, number of inoculated mice.
‡One animal got sick at 319 days, and two animals presented signs of ataxia at 370 days.
§The incubation period of the five sick mice was 412 ± 18 days.

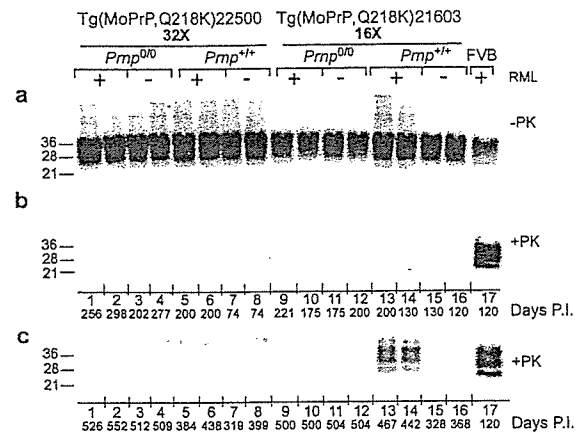

Fig. 4. Immunoblots of inoculated Tg(MoPrP,Q218K) mice. Brain homogenates were analyzed before (*a*) and after (*b* and *c*) limited PK digestion. Plus (+) and minus (−) signs indicate that mice were and were not inoculated, respectively, with RML prions. Membranes were probed with HuM-D13 Fab at a final concentration of 1 μg/ml. The numbers to the left of each blot indicate the molecular mass of protein standards in kDa. The number of days elapsed before the animal became ill or was killed is indicated as Days P.I. (*a* and *b*) Brain homogenates of mice at ≈200 days. Lanes 1–4, Tg(MoPrP,Q218K)22500/*Prnp*$^{0/0}$ mice that fell ill (lanes 1 and 3) or remained healthy and were killed (lanes 2 and 4); lanes 5–8, healthy Tg(MoPrP,Q218K)22500/*Prnp*$^{+/+}$ mice killed at the days indicated; lanes 9–12, healthy Tg(MoPrP,Q218K)21603/*Prnp*$^{0/0}$ mice killed at the days indicated; lanes 13–16, healthy Tg(MoPrP,Q218K)21603/*Prnp*$^{+/+}$ mice killed at the days indicated; lane 17, inoculated FVB mouse that died after ≈120 days. (*c*) Brain homogenates of Tg(MoPrP,Q218K) mice at ≈500 days. Lanes 1–4, ill Tg(MoPrP,Q218K)22500/*Prnp*$^{0/0}$ mice; lanes 5–8, ill Tg(MoPrP,Q218K)22500/*Prnp*$^{+/+}$ mice; lanes 9–12, healthy Tg(MoPrP,Q218K)21603/*Prnp*$^{0/0}$ mice killed at the days indicated; lanes 13–16, Tg(MoPrP,Q218K)21603/*Prnp*$^{+/+}$ mice that either fell ill (lanes 13 and 14) or were killed while still healthy (lanes 15 and 16); lane 17, inoculated FVB mouse that died after ≈120 days.

before and after PK digestion (Fig. 4 *a* and *b*). None of the samples from young mice with the *Prnp*$^{0/0}$ or *Prnp*$^{+/+}$ background showed detectable levels of PrP^{Sc} regardless of whether the animals were inoculated with RML prions (Fig. 4*b*). These samples were tested by CDI, and resulting D/N ratios were always below the 1.67 cut-off value for PrP^{Sc} (data not shown). Additional samples from Tg mice were taken between 319 and 552 days after inoculation for analysis. Protease-digested brain homogenates from ill Tg(MoPrP, Q218K)21603/*Prnp*$^{+/+}$ mice revealed low amounts of PrP^{Sc} (Fig. 4*c*, lanes 13 and 14), whereas PK-digested samples from ill Tg(MoPrP,Q218K)22500/*Prnp*$^{+/+}$ mice did not (Fig. 4*c*, lanes 5 and 6).

From these findings, we conclude that inoculated Tg(MoPrP,Q218K)22500/*Prnp*$^{+/+}$ mice developed CNS dysfunction not from prion accumulation but from overexpression of the transgene product. The presence of low but readily detectable amounts of PrP^{Sc} in inoculated, ill Tg(MoPrP,Q218K)21603/*Prnp*$^{+/+}$ mice raises the possibility that these mice developed prion disease. Presumably the lower level of MoPrP(Q218K) expression in Tg(MoPrP,Q218K)21603/*Prnp*$^{+/+}$ mice compared with Tg(MoPrP,Q218K)22500/*Prnp*$^{+/+}$ mice permitted prion replication to occur. Why the levels of PrP^{Sc} are not higher in the ill Tg(MoPrP,Q218K)21603/*Prnp*$^{+/+}$ mice is unknown. One argument is that these mice died of brain degeneration caused by the accumulation of the transgene product, but none of the other Tg(MoPrP,Q218K)21603 mice developed CNS illness (Table 2). Alternatively, relatively low levels of PrP^{Sc} might have caused illness or the combined presence of PrP^{Sc} and mutant MoPrP(Q218K) produced disease.

Discussion

The discovery of dominant-negative inhibition of prion replication began with the finding that chimeric HuM PrP transgenes rendered mice susceptible to human prions (33, 34). Using scrapie-infected neuroblastoma cells, we mapped the residues on PrP^{C} that are critical for dominant-negative inhibition of prion replication (19). The side chains of these residues on the surface of PrP^{C} form a discontinuous epitope near the C terminus, which is thought to bind to a macromolecule provisionally designated protein X. The avid binding of dominant-negative PrP to protein X is presumed to result in the sequestering of the protein, which in turn prevents conversion of wt PrP^{C} into PrP^{Sc}.

Scrapie-infected neuroblastoma-cell studies and investigations of naturally occurring PrP polymorphisms in sheep and humans that protect them from prion diseases argued for dominant-negative inhibition of prion replication. Although these polymorphisms may be more effective in the context of the ovine or human sequence, we postulated that experimental testing of this hypothesis in Tg mice would allow better characterization of the protective effects of dominant-negative variants. We produced mice expressing mutant MoPrP transgenes that carry either polymorphic residue protecting sheep or humans. The substitution of arginine at codon 167 or lysine at 218 rendered MoPrP^{C} unconvertible into PrP^{Sc}. When the transgene product and wt MoPrP^{C} were coexpressed, prion formation was retarded.

Dominant-Negative Inhibition of Scrapie. At codon 171, both heterozygous Q/R and homozygous R/R Suffolk sheep were found to be resistant to natural scrapie (17). In studies of experimental scrapie, Cheviot sheep carrying Q/R or R/R at residue 171 were found to be resistant to prion infection (16, 35–37). Similar findings have been reported for flocks of Texel sheep with natural scrapie. Sheep expressing ARR/ARR or ARR/AHQ at positions 136, 154, and 171, respectively, were the most resistant to scrapie, with 89% of animals surviving; sheep expressing VRQ/VRQ, ARQ/VRQ, or ARH/VRQ were the most susceptible to disease, with only 5% unaffected (38, 39). These findings are readily explained by our results with Tg(MoPrP,Q167R)*Prnp*$^{+/+}$ mice; position 167 in MoPrP corresponds to 171 in sheep PrP. Therefore, we conclude that protection of sheep expressing Q/R at position 171 from scrapie is caused by dominant-negative inhibition. Sheep expressing R/R at 171 were protected also because MoPrP(Q167R) was not converted into PrP^{Sc} even after 500 days after prion inoculation.

Dominant-Negative Inhibition of Prion Disease in Humans. Among the Japanese population, 12% carry the E/K polymorphism at position 219, whereas remaining individuals are E/E. None of 85 autopsied sporadic Creutzfeldt–Jakob disease cases were found to be E/K, suggesting that heterozygosity at 219 protects humans from this disease (40, 41). These findings are readily explained by our results with Tg(MoPrP,Q218K)*Prnp*$^{+/+}$ mice; position 218 in MoPrP corresponds to 219 in HuPrP. Thus, protection of humans expressing E/K at codon 219 from Creutzfeldt–Jakob disease is caused by dominant-negative inhibition.

Transgene Expressions Levels and Dominant-Negative Inhibition. In planning the studies described here, we sought to produce one mouse line with relatively low levels of mutant PrP expression and at least one line with high levels of mutant PrP expression. Tg(MoPrP,Q167R)*Prnp*$^{0/0}$ mice express MoPrP(Q167R) at about the same level that FVB mice express wt MoPrP. Tg(MoPrP,Q218K)21603/*Prnp*$^{0/0}$ and Tg(MoPrP,Q218K)22500/*Prnp*$^{0/0}$ mice express MoPrP(Q218K) at 16 and 32×, respectively. Although none of the uninoculated Tg(MoPrP,Q167R)*Prnp*$^{0/0}$ and Tg(MoPrP,Q218K)21603/*Prnp*$^{0/0}$ mice developed spontaneous neurologic disease, 18 of 26 Tg(MoPrP,Q218K)22500/*Prnp*$^{0/0}$ mice developed what appears to be spontaneous neurodegeneration (Table 2).

Although Tg(MoPrP,Q167R)*Prnp*$^{+/+}$ mice were asymptomatic at 300 days after inoculation with RML prions, their brains contained detectable levels of PrP^{Sc} (Figs. 2 and 3). Presumably, PrP^{Sc}

was derived from wt PrP^C, but we have no antibodies that distinguish wt PrP^{Sc} from putative PrP^{Sc}(Q167R). However, our results clearly show the inhibitory effect of MoPrP(Q167R) on the conversion of wt PrP^C into PrP^{Sc} as reflected by the prolonged incubation times in Tg(MoPrP,Q167R)*Prnp*$^{+/+}$ mice compared with FVB mice (Table 1).

Tg(MoPrP,Q218K)21603/*Prnp*$^{+/+}$ and Tg(MoPrP,Q218K)-22500/*Prnp*$^{+/+}$ mice reacted differently to inoculation with prions. After incubation times as long as 500 days, Tg(MoPrP,Q218K)22500/*Prnp*$^{+/+}$ mice were unable to form nascent wt PrP^{Sc}, whereas Tg(MoPrP,Q218K)21603/*Prnp*$^{+/+}$ mice developed CNS dysfunction at 412 ± 18 days and exhibited low levels of PrP^{Sc} (Fig. 4*c*). This result is most readily explained by the different levels of transgene expression. Whether Tg(MoPrP,Q218K)21603/*Prnp*$^{+/+}$ mice became ill because of prion disease remains uncertain. One possibility is that the neurologic disease seen in these mice is caused by combined effects of PrP^{Sc} accumulation and the high level of MoPrP(Q218K) expression. Certainly MoPrP(Q218K) expression alone in Tg(MoPrP,Q218K)21603/*Prnp*$^{0/0}$ mice does not seem sufficient to cause disease (Table 2), and low levels of wt $MoPrP^{Sc}$ are generally not associated with clinical signs or neuropathologic changes (Fig. 4*c*).

Prevention of Prion Disease. The inability of MoPrP(Q167R) and MoPrP(Q218K) to support prion replication raises the possibility of producing prion-resistant livestock that express PrP with a single amino acid substitution. Because sheep homozygous for R at position 171 already exist, breeding populations of resistant sheep is a reasonable undertaking. Presumably, this was the genetic basis of Parry's scrapie eradication program in Great Britain 40 years ago (42, 43). However, this natural protection might be restricted to certain prion strains. Recently, experimental transmission of bovine spongiform encephalopathy prions to sheep showed that animals carrying ARQ/ARQ at codon 136, 154, and 171, respectively, died after 672 days, whereas sheep harboring ARR/ARR were resistant to bovine spongiform encephalopathy prions (44). The ARR/ARR sheep showed neither neurologic signs nor PrP^{Sc} deposits in their brains. It would seem prudent to explore the utility of such an approach by inoculating Tg(ShePrP,Q171R)*Prnp*$^{0/0}$ mice with many different prion strains. A similar approach, inoculating Tg(BoPrP,Q179R)*Prnp*$^{0/0}$ or Tg(BoPrP,Q230K)*Prnp*$^{0/0}$ mice with many different prion strains, might be useful in evaluating the utility of producing prion-resistant cattle. Although the introduction of a point mutation may not produce complete resistance to prion infection as disruption of the *Prnp* gene does (45, 46), it may prove to be more desirable. Whether disruption of the *Prnp* gene produces some subtle but important aberration in cattle, sheep, or pigs is unknown; moreover, such livestock may be considered unacceptable to consumers. In contrast, the introduction of a naturally occurring point mutation may be less detrimental biologically and accepted more readily by consumers. Both germ-line and somatic cell gene therapy strategies could be applied in principle.

Should single point mutations in sheep or bovine PrP transgenes prove to be ineffective with some strains, it may be prudent to construct a transgene carrying both substitutions. Whether Tg mice expressing BoPrP(Q179R,Q230K) will be healthy or develop spontaneous neurodegeneration is unknown (32). Moreover, whether such mice will be more resistant to prion disease remains to be established.

We thank Jeff Monaghan for his excellent technical support with the Tg mice screening. This work was supported by grants from the National Institutes of Health as well as a gift from the G. Harold and Leila Y. Mathers Foundation. V.P. received fellowships from the Fondation pour la Recherche Médicale and the French Alzheimer's Foundation.

1. DeArmond, S. J., Mobley, W. C., DeMott, D. L., Barry, R. A., Beckstead, J. H. & Prusiner, S. B. (1987) *Neurology* **37**, 1271–1280.
2. Korth, C., May, B. C. H., Cohen, F. E. & Prusiner, S. B. (2001) *Proc. Natl. Acad. Sci. USA* **98**, 9836–9841.
3. Doh-ura, K., Iwaki, T. & Caughey, B. (2000) *J. Virol.* **74**, 4894–4897.
4. Supattapone, S., Nguyen, H.-O. B., Cohen, F. E., Prusiner, S. B. & Scott, M. R. (1999) *Proc. Natl. Acad. Sci. USA* **96**, 14529–14534.
5. Caughey, W. S., Raymond, L. D., Horiuchi, M. & Caughey, B. (1998) *Proc. Natl. Acad. Sci. USA* **95**, 12117–12122.
6. Demaimay, R., Harper, J., Gordon, H., Weaver, D., Chesebro, B. & Caughey, B. (1998) *J. Neurochem.* **71**, 2534–2541.
7. Perrier, V., Wallace, A. C., Kaneko, K., Safar, J., Prusiner, S. B. & Cohen, F. E. (2000) *Proc. Natl. Acad. Sci. USA* **97**, 6073–6078.
8. Soto, C., Kascsak, R. J., Saborío, G. P., Aucouturier, P., Wisniewski, T., Prelli, F., Kascsak, R., Mendez, E., Harris, D. A., Ironside, J., *et al.* (2000) *Lancet* **355**, 192–197.
9. Peretz, D., Williamson, R. A., Kaneko, K., Vergara, J., Leclerc, E., Schmitt-Ulms, G., Mehlhorn, I. R., Legname, G., Wormald, M. R., *et al.* (2001) *Nature (London)* **412**, 739–743.
10. Enari, M., Flechsig, E. & Weissmann, C. (2001) *Proc. Natl. Acad. Sci. USA* **98**, 9295–9299.
11. Priola, S. A., Raines, A. & Caughey, W. S. (2000) *Science* **287**, 1503–1506.
12. Schenk, D., Barbour, R., Dunn, W., Gordon, G., Grajeda, H., Guido, T., Hu, K., Huang, J., Johnson-Wood, K., Khan, K., *et al.* (1999) *Nature (London)* **400**, 173–177.
13. Bard, F., Cannon, C., Barbour, R., Burke, R.-L., Games, D., Grajeda, H., Guido, T., Hu, K., Huang, J., Johnson-Wood, K., *et al.* (2000) *Nat. Med.* 916–919.
14. DeMattos, R. B., Bales, K. R., Cummins, D. J., Dodart, J. C., Paul, S. M. & Holtzman, D. M. (2001) *Proc. Natl. Acad. Sci. USA* **98**, 8850–8855.
15. Birmingham, K. & Frantz, S. (2002) *Nat. Med.* **8**, 199–200.
16. Goldmann, W., Hunter, N., Smith, G., Foster, J. & Hope, J. (1994) *J. Gen. Virol.* **75**, 989–995.
17. Westaway, D., Zuliani, V., Cooper, C. M., Da Costa, M., Neuman, S., Jenny, A. L., Detwiler, L. & Prusiner, S. B. (1994) *Genes Dev.* **8**, 959–969.
18. Shibuya, S., Higuchi, J., Shin, R.-W., Tateishi, J. & Kitamoto, T. (1998) *Ann. Neurol.* **43**, 826–828.
19. Kaneko, K., Zulianello, L., Scott, M., Cooper, C. M., Wallace, A. C., James, T. L., Cohen, F. E. & Prusiner, S. B. (1997) *Proc. Natl. Acad. Sci. USA* **94**, 10069–10074.
20. Zulianello, L., Kaneko, K., Scott, M., Erpel, S., Han, D., Cohen, F. E. & Prusiner, S. B. (2000) *J. Virol.* **74**, 4351–4360.
21. Telling, G. C., Haga, T., Torchia, M., Tremblay, P., DeArmond, S. J. & Prusiner, S. B. (1996) *Genes Dev.* **10**, 1736–1750.
22. Chandler, R. L. (1961) *Lancet* **1**, 1378–1379.
23. Carlson, G. A., Goodman, P. A., Lovett, M., Taylor, B. A., Marshall, S. T., Peterson-Torchia, M., Westaway, D. & Prusiner, S. B. (1988) *Mol. Cell. Biol.* **8**, 5528–5540.
24. Carlson, G. A., Kingsbury, D. T., Goodman, P. A., Coleman, S., Marshall, S. T., DeArmond, S., Westaway, D. & Prusiner, S. B. (1986) *Cell* **46**, 503–511.
25. Scott, M., Foster, D., Mirenda, C., Serban, D., Coufal, F., Wälchli, M., Torchia, M., Groth, D., Carlson, G., DeArmond, S. J., *et al.* (1989) *Cell* **59**, 847–857.
26. Supattapone, S., Muramoto, T., Legname, G., Mehlhorn, I., Cohen, F. E., DeArmond, S. J., Prusiner, S. B. & Scott, M. R. (2001) *J. Virol.* **75**, 1408–1413.
27. Serban, D., Taraboulos, A., DeArmond, S. J. & Prusiner, S. B. (1990) *Neurology* **40**, 110–117.
28. Scott, M. R., Köhler, R., Foster, D. & Prusiner, S. B. (1992) *Protein Sci.* **1**, 986–997.
29. Safar, J., Wille, H., Itri, V., Groth, D., Serban, H., Torchia, M., Cohen, F. E. & Prusiner, S. B. (1998) *Nat. Med.* **4**, 1157–1165.
30. Muramoto, T., Kitamoto, T., Tateishi, J. & Goto, I. (1992) *Am. J. Pathol.* **140**, 1411–1420.
31. Taraboulos, A., Jendroska, K., Serban, D., Yang, S.-L., DeArmond, S. J. & Prusiner, S. B. (1992) *Proc. Natl. Acad. Sci. USA* **89**, 7620–7624.
32. Westaway, D., DeArmond, S. J., Cayetano-Canlas, J., Groth, D., Foster, D., Yang, S.-L., Torchia, M., Carlson, G. A. & Prusiner, S. B. (1994) *Cell* **76**, 117–129.
33. Telling, G. C., Scott, M., Hsiao, K. K., Foster, D., Yang, S.-L., Torchia, M., Sidle, K. C. L., Collinge, J., DeArmond, S. J. & Prusiner, S. B. (1994) *Proc. Natl. Acad. Sci. USA* **91**, 9936–9940.
34. Telling, G. C., Scott, M., Mastrianni, J., Gabizon, R., Torchia, M., Cohen, F. E., DeArmond, S. J. & Prusiner, S. B. (1995) *Cell* **83**, 79–90.
35. Clousard, C., Beaudry, P., Elsen, J. M., Milan, D., Dussaucy, M., Bounneau, C., Schelcher, F., Chatelain, J., Launay, J.-M. & Laplanche, J.-L. (1995) *J. Gen. Virol.* **76**, 2097–2101.
36. Bossers, A., Schreuder, B. E. C., Muileman, I. H., Belt, P. B. G. M. & Smits, M. A. (1996) *J. Gen. Virol.* **77**, 2669–2673.
37. Hunter, N., Cairns, D., Foster, J. D., Smith, G., Goldmann, W. & Donnelly, K. (1997) *Nature (London)* **386**, 137.
38. Belt, P. B. G. M., Muileman, I. H., Schreuder, B. E. C., Ruijter, J. B., Gielkens, A. L. J. & Smits, M. A. (1995) *J. Gen. Virol.* **76**, 509–517.
39. Baylis, M., Houston, F., Goldmann, W. & McClean, A. (2000) in *International Symposium on Prion Diseases and Related Processes* (Fondation Marcel Mérieux, Les Pensières, Veyrier-du-Lac, France).
40. Kitamoto, T. & Tateishi, J. (1994) *Philos. Trans. R. Soc. London B* **343**, 391–398.
41. Shibuya, S., Higuchi, J., Shin, R.-W., Tateishi, J. & Kitamoto, T. (1998) *Lancet* **351**, 419.
42. Parry, H. B. (1962) *Heredity* **17**, 75–105.
43. Parry, H. B. (1983) in *Scrapie Disease in Sheep*, ed. Oppenheimer, D. R. (Academic, New York), pp. 31–59.
44. Baron, T. G., Madec, J. Y., Calavas, D., Richard, Y. & Barillet, F. (2000) *Neurosci. Lett.* **284**, 175–178.
45. Büeler, H., Aguzzi, A., Sailer, A., Greiner, R.-A., Autenried, P., Aguet, M. & Weissmann, C. (1993) *Cell* **73**, 1339–1347.
46. Prusiner, S. B., Groth, D., Serban, A., Koehler, R., Foster, D., Torchia, M., Burton, D., Yang, S.-L. & DeArmond, S. J. (1993) *Proc. Natl. Acad. Sci. USA* **90**, 10608–10612.

THE JOURNAL OF BIOLOGICAL CHEMISTRY
Vol. 277, No. 33, Issue of August 16, pp. 30382–30387, 2002
Printed in U.S.A.

In Situ Phage Screening

A METHOD FOR IDENTIFICATION OF SUBNANOGRAM TISSUE COMPONENTS *IN SITU*[*]

Received for publication, April 12, 2002, and in revised form, May 29, 2002
Published, JBC Papers in Press, June 4, 2002, DOI 10.1074/jbc.M203547200

Torahiko Tanaka‡§, Takashi Ito‡§, Masaru Furuta‡§, Chikashi Eguchi‡§, Hiroyuki Toda‡§¶, Eriko Wakabayashi-Takai‡§, and Kiyotoshi Kaneko‡§‖

From the ‡Department of Cortical Function Disorders, National Institute of Neuroscience, National Center of Neurology and Psychiatry, 4-1-1 Ogawahigashi, Kodaira, Tokyo 187-8502, the ¶Department of Neurology, Yokohama City University School of Medicine, 3-9 Fukuura, Kanazawa-ku, Yokohama 236-0004, and the §Core Research for Evolutional Science and Technology, Japan Science and Technology Corporation, Kawaguchi, Saitama 332-0012, Japan

We have established a novel method, *in situ* phage screening (ISPS), to identify proteins in tissue microstructures. The method is based on the selection of repertoires of phage-displayed antibody fragments with small samples of tissues microdissected using a laser. Using a human muscle frozen section with an area of 4800 μm^2 as a model target, we successfully selected monoclonal antibody fragments directed against three major (myosin heavy chain, actin, and tropomyosin-α) and one minor (α-actinin 2) muscle constituent proteins. These proteins were present in the sample in amounts less than one nanogram, and the antibodies were used to visualize the proteins *in situ*. This shows that the use of ISPS can obtain monoclonal antibodies for histochemical and biochemical purposes against minute amounts of proteins from microstructures with no requirement for large amounts of samples or biochemical efforts.

In the post-genomic era, nanoscale technologies such as femtomole-ranged mass spectrometry (1) have become indispensable for proteomic analyses to clarify changes in protein components and abnormality of protein functions in human diseases. Here, we describe a novel nanoscale method, *in situ* phage screening (ISPS),[1] which enables us to identify protein components in microstructures seen with microscopy. The method involves the combination of phage antibody display technology (2–5) with laser microdissection technology (6, 7). For these purposes, we used a library of single chain variable fragments (scFv) of antibodies (2, 3) fused to gene III of M13 phage and expressed at the tip of the phage particles (3, 8). For microdissection of tissues, we developed a new laser-microdissector by combining an industrial-use laser cutter and an inverted microscope. The procedure involves isolation of the target microstructures from the surrounding tissues *on glass* by dissection and then incubation with the phage antibody library. Phage antibodies were isolated after a single round of selection, and their specificities were identified by immunohistochemistry and Western blotting. Target antigens were identified by immunoscreening of cDNA expression libraries using the monoclonal phage antibodies.

The clinical targets of ISPS are those characterized by abnormal or yet unknown protein accumulations, which closely relate with pathogenetic mechanisms, such as subcutaneous deposits or inclusion bodies and extracellular plaques often seen in neuromuscular and other degenerative diseases. ISPS is highly advantageous when the target microstructures can hardly be collected by standard biochemical methodologies; for instance, targets are very small (up to 1 μm in size) or rare (seen in few cells), or they appear in complex pathophysiological structures.

Because muscle cells consist of relatively small numbers of proteins, we employed human skeletal muscle as a model target of ISPS. In this report, we describe model experiments of ISPS on human muscle, where we successfully identified the three major and one minor muscle antigens from an area of 4800-μm^2 microfragments.

EXPERIMENTAL PROCEDURES

scFv Phage Library and Production of Recombinant Phages—A human synthetic scFv library "Griffin. 1" (9) was provided from Dr. G. Winter (Medical Research Council, UK) and amplified in our laboratory. In this library, the VH and VL sequence connected with a spacer sequence (3, 8) was inserted into an *NcoI-NotI* restriction site and followed by the M13 gene III sequence in phagemid vector pHEN2. Recombinant scFv phages were rescued in *Escherichia coli* suppressor strain TG1 in the presence of helper phage VCSM13 (Stratagene Cloning System, La Jolla, CA) as described previously (9, 10).[2] Briefly, bacteria carrying scFv phagemid were cultured in a 2× YT medium (11) containing 100 μg/ml ampicillin and 1% glucose and infected in the log phase (absorbance at 600 nm (A_{600}) was 0.5) with VCSM13 at a ratio of 1:20 (number of bacterial cells/phage particles) for 30 min at 37 °C without shaking. The bacteria were pelleted by centrifugation, resuspended in a 2× YT medium containing 100 μg/ml ampicillin and 25 μg/ml kanamycin (4 volumes of the original), and grown overnight at 30 °C. Phages were purified from the culture supernatant by polyethylene glycol precipitation (2) and resuspended in TBS (20 mM Tris-Cl, pH 7.6, 0.15 M NaCl). The working solution of the phage library was prepared at the concentration of 10^{13} colony forming units (cfu)/ml. An anti-thyroglobulin scFv phage was also provided by Dr. G. Winter.

Selection of scFv Phages in Situ—Histologically normal biopsy specimens of skeletal muscle (biceps brachii) were provided by the NCNP research resource network (Kodaira, Tokyo) after obtaining the informed consent of the patients. Transverse (experiments A and B) and

* This work is supported by grants from the Ministry of Health, Labor and Welfare and the Ministry of Education, Culture, Sports, Science and Technology (Core Research for Evolutional Science and Technology and grant-in-aid for scientific research), Japan. The costs of publication of this article were defrayed in part by the payment of page charges. This article must therefore be hereby marked "*advertisement*" in accordance with 18 U.S.C. Section 1734 solely to indicate this fact.

‖ To whom correspondence should be addressed. Tel.: 81-42-346-1718; Fax: 81-42-346-1748; E-mail:kaneko@ncnp.go.jp.

[1] The abbreviations used are: ISPS, *in situ* phage screening; Fv, variable fragment of immunoglobulin; scFv, single chain Fv; VH, heavy chain variable region; VL, light chain variable region; cfu, colony forming units; GFAP, glial fibrillary acidic protein; NCNP, National Center of Neurology and Psychiatry; HRP, horseradish peroxidase; CHAPS, 3-[(3-cholamidopropyl)dimethylammonio]-1-propanesulfonic acid; IPG, immobilized pH gradient; MALDI-TOF, matrix-assisted laser desorption ionization time-of-flight; MS, mass spectrometry.

[2] Details of the Griffin. 1 library and phage protocols are also given on the Winter group home page (www.mrc-cpe.cam.ac.uk/phage/index.html).

longitudinal (experiments C through E) frozen sections that were 2-μm thick were cut with a cryostat, attached to silanized slides (Dako), and subjected to laser microdissection. Spaces 15 μm wide surrounding 40 × 40-μm square microfragments were made with pulsed shots of the ultraviolet laser. After the sections were immersed in acetone for 5 min and air-dried, they were blocked with TBS-10% (weight/volume) skim milk for 2 h and then incubated with the phage library (5×10^{11} cfu in 50 μl of TBS in experiments A and B or in 75 μl of TBS-10% skim milk in experiments C through E) for 12 h at room temperature. After washing with TBS-0.05% Tween 20 (TBS-T) four times ×30 min, the sections were overlaid with 0.2 ml of TBS-T. Three microfragments of 40 × 40 μm were then collected into a microcentrifuge tube with a hand-made micropipette (inner diameter, 60–80 μm) together with a minimal amount of overlaid TBS-T, and the microfragments were washed three times by brief centrifugation with 0.2 ml of TBS-T each. After washing, the contents of the tube were examined microscopically to determine whether the three microfragments remained in the tube.

In the direct colony recovery protocol, phages were eluted from the pelleted fragments with 100 μl of 1.4% triethylamine for 10 min at room temperature with vigorous shaking followed by neutralization with 50 μl of 1 M Tris-Cl, pH 7.4. A TG1 culture (1 ml) in the log phase (A_{600} = 0.5) was infected with the eluted phage solution for 30 min at 37 °C and plated on LB-agar (11) containing 100 μg/ml ampicillin and 1% glucose. All of the ampicillin-resistant colonies obtained, which were carrying scFv phagemid, were subjected to the analysis of specificity.

In the PCR fragment-subcloning protocol, the three pelleted microfragments were suspended in 10 μl of water, heated at 95 °C for 5 min, and then rapidly cooled in ice. The Fv sequences derived from the phages bound to the microfragments were amplified by PCR using forward (5′-CGGATAACAATTTCACACAGGAAAC-3′) and reverse (5′-CTATGCGGCCCCATTCAGATC-3′) primers. The reaction (50 μl) contained 5 μl of a 10-fold-concentrated *Taq* reaction buffer (Takara, Japan), 0.8 μM each of the forward and reverse primers, 0.2 mM dNTPs (Takara, Japan), the heat-treated sample (10 μl as described above), and 2.5 units of *Taq* polymerase (Takara, Japan) and was kept in ice. After heating at 98 °C for 1 min, 38 cycles of PCR (60 °C for 20 s, 72 °C for 1 min, and 95 °C for 20 s) were performed and followed by incubation at 72 °C for 3 min. The PCR product (0.95 kbp) was digested with *Nco*I and *Not*I, ligated with *Nco*I- and *Not*I-digested pHEN2, and transformed into TG1. The bacteria were plated to form ampicillin-resistant colonies. It was confirmed that no PCR products were obtained by using the final wash supernatant of the muscle microfragment (see Fig. 1). A portion of the colonies was subjected to analysis of scFv specificity.

Specificity of scFv Phages—The Fv sequence in each colony was amplified by PCR (30 cycles of 95 °C for 15 s, 60 °C for 15 s, and 72 °C for 1 min) using the same primer set as described above, digested with *Hae*III, and electrophoresed on 4.5% agarose for fingerprinting. The monoclonal phage was rescued from the representative clones showing unique patterns on fingerprinting and analyzed immunohistochemically and by Western blotting. For immunostaining, muscle frozen-sections preblocked with TBS-10% skim milk were incubated with one to four unique phages (5×10^{10} cfu each in 100 μl of TBS-10% skim milk) simultaneously for 12 h at room temperature. After washing twice with TBS-T for 15 min, the sections were incubated with 1000-fold-diluted anti-M13 mouse IgG (Progen Biotechnik, Heidelberg) in TBS-5% skim milk for 1 h. After washing twice as above, the sections were stained by using an Envision-HRP kit (Dako) according to the manufacturer's protocol. For Western blotting, muscle sections (about 25–50 μg as protein) were dissolved in a 2-fold-concentrated sample buffer of SDS-PAGE (11), electrophoresed on 10% preparative gel, and transferred to a nitrocellulose membrane. The membrane was cut into strips 1–3 mm wide, blocked with 10% skim milk in TBS for 1 h, and incubated with scFv phages in TBS-10% skim milk for 2 h. In another set of experiments (with Tween treatment), the membrane strips were incubated with TBS-0.1% Tween 20 for 1 h, followed by blocking and phage incubation as described above, but in the presence of 0.1% Tween 20 (12). After washing with TBS-0.1% Tween 20 for 10 min six times, the strip was incubated with 10,000-fold-diluted anti-M13 mouse IgG-HRP conjugated (Amersham Biosciences) in TBS-0.1% Tween 20 for 1 h. After washing with TBS-0.1% Tween 20 as above, the blot was visualized with an ECL Plus Western blotting detection system (Amersham Biosciences).

Two-dimensional Western Blotting and Mass Fingerprinting Analysis—Muscle sections (about 30 and 300 μg as protein for Western and mass analysis, respectively) were dissolved in 250 μl of a two-dimensional gel electrophoresis buffer (20 mM Tris base, 9 M urea, 2 M thiourea, 4% CHAPS, 65 mM dithioerythritol, and 0.5% immobilized pH gradient (IPG) buffer (Amersham Biosciences)) and subjected to isoelectric focusing by using an IPGphor system (Amersham Biosciences) with a 13 cm-long IPG strip (pH range, 3–10) according to the manufacturer's protocol. The IPG strip was then applied to the top of an SDS-PAGE gel (7.5%, 14 × 12 cm). For mass fingerprinting analysis, proteins on the two-dimensional gel were visualized by using a copper-staining kit (Bio-Rad). The target protein spots were then cut out, digested in gel with trypsin, and analyzed with a MALDI-TOF (matrix-assisted laser desorption ionization-time of flight) type mass spectrometer (Voyager-DEPRO, Applied Biosystems) (1, 13). The peptide mass fingerprinting analysis was performed by using the program MS-FIT. Western analysis was carried out as described above.

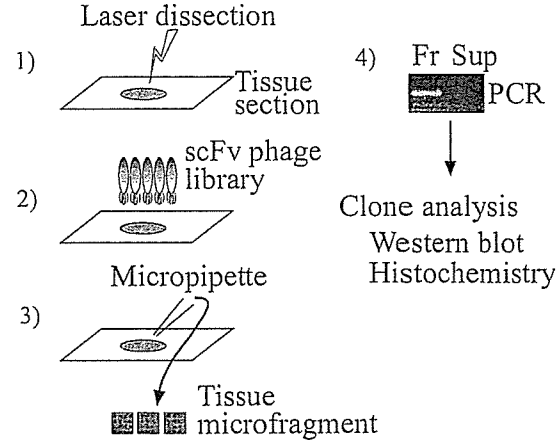

FIG. 1. **Schematic presentation of *in situ* phage screening (ISPS).** ISPS is performed by laser-dissection and isolation of target microstructures from surrounding tissues on a tissue section (*1*), incubation of the tissue section with an scFv phage library (*2*), collection of targets (*3*), and rescue of the bound phages and selection of target-specific phages (*4*). The scFv sequences of phages bound to microfragments were amplified by PCR (*Fr*) and subcloned into phagemid vector pHEN2 (see "Experimental Procedures"). No PCR products were obtained from wash supernatant of the microfragments (*Sup*), indicating that the bound phages were not contaminated by those from residual tissues other than the microfragments.

Immunoscreening of the Human Muscle cDNA Expression Library—A human skeletal muscle 5′-STRETCH PLUS cDNA library (CLONTECH, Palo Alto, CA) was immunoscreened according to the manufacturer's protocol by using scFv phages. Library plaques were transferred to nitrocellulose membranes, incubated with scFv phages (5×10^{10} cfu/ml, for 2 h), and visualized by using anti-M13 mouse IgG-HRP conjugated and ECL Plus Western blotting detection reagent (Amersham Biosciences) as described above.

RESULTS

Optimal Conditions for ISPS in Muscle—ISPS is performed by 1) dissection and isolation of target microstructures from surrounding tissues on a tissue section, 2) incubation of the tissue section with an scFv phage library, 3) collection of targets, and 4) selection of target-specific phages (Fig. 1). A new laser microdissector was developed to cut out the microstructures under a microscope (Fig. 2*A*). The dissector produced a rectangular space of variable size (1–56 μm) on a tissue section with a single shot of an ultraviolet laser beam at 266 nm (Fig. 2*B*). Tissues surrounding the target were widely burnt off by precisely controlling the laser power. Spaces that were 15 μm wide surrounding a 40 × 40-μm^2 square microfragment were usually produced in a muscle section by the dissector (Fig. 2*C*). As a source of scFvs, we employed a phagemid library, Griffin. 1 (see "Experimental Procedures"). The scFv sequences were constructed with synthetic human V-gene sequences of immunoglobulin, VH and VL (3, 8). When the phages were rescued by using helper phages derived from M13 (VCSM13), the V-gene was fused with the gene III of the M13 phage and expressed as an scFv at the tip of the phage particle (2). The Griffin. 1 library contained about 10^9 independent unique clones (9).

We first determined the optimal conditions for phage anti-

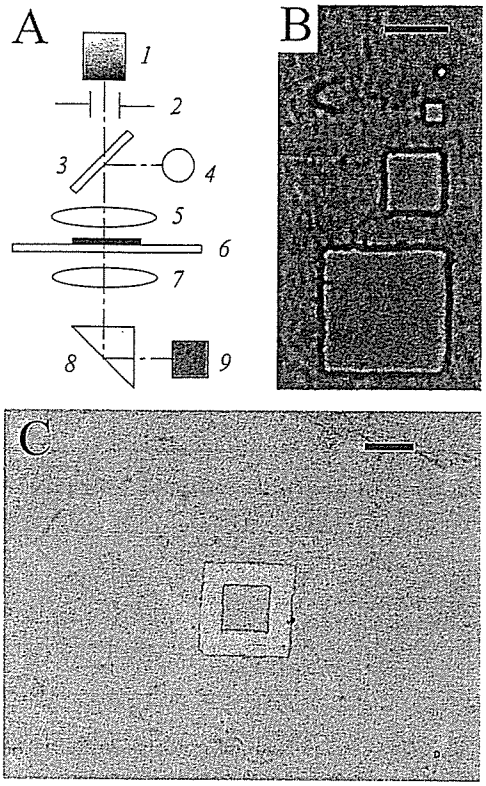

FIG. 2. *A*, a diagram of a new laser microdissector constructed by combining a UV laser system (HCL-2100SUV, Hoya Continuum Co., Ltd., Japan) and an inverted research microscope (IX70, Olympus Optical Co., Ltd., Japan). *1*, UV laser head; *2*, slit; *3*, dichroic mirror; *4*, halogen lamp; *5*, objective (UV laser); *6*, sample slide; *7*, objective (observation); *8*, prism (light path switch); *9*, charge-coupled device camera. *B*, *square spaces* burnt into a muscle frozen-section by the dissector. *Scale bar*, 10 μm. From the *top*: 1-, 3-, 10-, and 20-μm^2 squares. *C*, A 40 × 40-μm square muscle microfragment fractioned in a frozen section with the dissector. The section was stained with hematoxylin to demonstrate the architecture of muscle. The *scale bar* represents 40 μm.

body reaction with muscle microfragments. Anti-human α-actin and anti-human glial fibrillary acidic protein (GFAP) phages (designated Actin89 and GFAP53, respectively) were obtained from the Griffin. 1 library by the conventional panning method using polystyrene tubes (10). Actin89 phage was used for the evaluation of specific binding to muscle microfragments, and GFAP53 phage was used for that of nonspecific binding, because GFAP is an astrocyte-specific protein. After reacting these phages with a muscle section, 3–5 microfragments (40 × 40-μm^2 square) were collected and washed three times to eliminate contamination by phages from residual tissues other than the microfragments. The phages bound to the microfragments were eluted with 1.4% triethylamine and allowed to infect *E. coli* TG1. The phage titer was measured as the number of ampicillin-resistant colonies (cfu). Skim milk was employed as a blocking agent because of findings in studies of muscle immunostaining with phage antibody in which 10% skim milk, but not 5%, worked well as a blocking agent. We checked the blocking effect of 10% skim milk on the nonspecific binding of GFAP53 phage to muscle fragments (Table I). As seen, preincubation with 10% skim milk or its presence during phage incubation was optimal in preventing the binding of unrelated phage GFAP53 to muscle fragments. Elevated amounts of nonspecific phage binding were only seen in the absence of the blocking agent throughout the experiment. Interestingly, the binding of Actin89 phage to muscle fragments was not affected either in the presence or absence of 10% skim milk (Table I).

TABLE I
Effect of skim milk on specific or non-specific phage binding to muscle microfragments

Muscle microfragments were incubated with or without 10% skim milk for 2 h (preblock) and incubated with Actin89 (10^{10} cfu/ml) or GFAP53 (10^{12} cfu/ml) phages with or without 10% skim milk for 12 h (incubation). Values represent mean ± S.D. (n = 3).

Skim milk		Phage recovery	
Preblock	Incubation	Actin89	GFAP53
		cfu/1000 μm^2	
+	+	11 ± 3	0.5 ± 0.2
−	+	ND[a]	0.6 ± 0.1
+	−	ND	0.2 ± 0.2
−	−	9 ± 6	8 ± 4

[a] ND, not determined.

We next checked the relation between input phage concentrations and amounts of phage binding to muscle fragments (Table II). As seen, the numbers of Actin89 phage bound to muscle microfragments were linearly related to the concentrations of input Actin89 phage (10^8–10^{12} cfu/ml) under optimal conditions. Similar linearity was observed when Actin89 was reacted with purified α-actin bound to an enzyme-linked immunosorbent assay plate (input 10^5–10^{12} cfu/ml, data not shown). When the input phage concentration was 10^{12} cfu/ml, the amount of Actin89 bound to the plate was 13,000 cfu/1000 μm^2. An anti-thyroglobulin phage was examined as an unrelated phage.

We also investigated the effect of the duration of incubation on the binding of Actin89 phage to a muscle microfragment. No significant difference was observed among the numbers of the phages collected after incubation for 3, 6, 12, and 60 h. The antigen retrieval effect of solvents on muscle microfragments was evaluated by quantifying the binding capacity of Actin89 to the microfragment. Among the solvents tested (acetone, methanol, ethanol, isopropanol, chloroform, sodium dodecyl sulfate (0.01 and 0.1%), Tween 20 (1%), and paraformaldehyde (2 and 4%)), acetone and ethanol pretreatment enhanced binding capacity the most, namely, three times more than in the absence of treatment. Acetone pretreatment was employed in the standard protocol for ISPS on human muscle.

Screening of the Griffin. 1 Library on a Micro Area of Muscle—We produced various size microfragments on a transverse section of human muscle by laser-dissection and incubated them with the Griffin. 1 library. The bound phages were directly eluted from microfragments and used to infect TG1 ("direct colony recovery" protocol), or the scFv sequences of bound phages were amplified by PCR and subcloned into phagemid vector pHEN2 ("PCR fragment subcloning" protocol). Phages were rescued from ampicillin-resistant colonies, and after unique clones were picked up by *Hae*III-fingerprinting, their specificity for muscle antigens was checked by both immunohistochemistry and Western blotting of muscle antigens.

The PCR fragment subcloning protocol yielded no phage clones from an area of 100 (10 × 10) μm^2 and three phage clones from 1100 (33 × 33) μm^2. The three phage clones from the 1100 μm^2 microfragment showed no specificity for muscle antigens, as judged by immunostaining. When the reaction area was enlarged to 4800 μm^2 (3 microfragments of 40 × 40 μm), we obtained a number of unique phage clones in two independent trials both by direct colony recovery and PCR fragment subcloning protocols (Table III, experiments A and B). The PCR fragment subcloning protocol gave us larger numbers of unique clones than the direct colony recovery protocol (Table III), because less than 1 cfu of phagemid was amplified under our PCR conditions. About 8 phage particles were equiv-

TABLE II
Relation between input phage concentration and phage recovery from muscle microfragments

Values represent mean ± S.D.

Phage input	Phage recovery		
	Actin89	GFAP53	Anti-thyroglobulin
cfu/ml	*cfu/1000 μm²*		
10^{12}	850 ± 300[a]	0.5 ± 0.2[b]	1.0 ± 0.4[b]
10^{11}	73 ± 31[a]	ND[c]	ND
10^{10}	15 ± 14[a]	ND	ND
10^{9}	0.8 ± 0.4[b]	ND	ND
10^{8}	0[b]	ND	ND

[a] $n=5$.
[b] $n=3$.
[c] ND, not determined.

TABLE III
Profile of in situ phage screening on 4800 μm² of muscle microfragments

Clones were selected from the Griffin. 1 library on transverse (A and B) or longitudinal muscle sections (C, D, and E) by a direct colony recovery protocol (direct) or a PCR fragment subcloning protocol (PCR).

Experiment	Number of clones		
	Analyzed	Unique	Positive
A			
Direct	3	3	0
PCR round 1	72	29	1
PCR round 2	24	8	1
B			
Direct	22	14	1
PCR round 1	72	47	1
PCR round 2	72	23	0
C PCR	48	13	2
D PCR	48	11	1
E PCR	48	9	3

alent to 1 cfu.[3] The two trials, A and B, yielded three positive clones, A28, B6, and B85, which specifically reacted with 37-, 100-, and 42-kDa muscle antigens, respectively (Tables III and IV and Fig. 3*A*). In PCR fragment subcloning experiments, the collected phages (round 1) were amplified and applied to the second round of selection (round 2) as in the same manner. In experiment A, the positive clone obtained from round 1 (A28) was again recovered in round 2; however, in experiment B, the positive clone in round 1 (B85) was not found in round 2 (Table III). This suggested that repeated panning steps sometimes lost positive clones that were present in the earlier round of phage pool.

We planned another series of experiments by using a longitudinal muscle section to obtain a homogeneous distribution at the reaction surface of muscle antigens which localized in muscle-specific, repeating zone structures such as the A- and I-bands. The screening was also performed on 4800-μm^2 microfragments by using the Griffin. 1 library. Three independent trials (experiments C, D, and E) yielded scFv clones reactive with 210-kDa protein (C43 and E2) and 42-kDa protein (C22, D2, E6, and E30) by the PCR fragment subcloning protocol (Tables III and IV). The results of one-dimensional Western analysis using the representative phage clones (A28, B6, E2, and E6) are demonstrated in Fig. 3*A*. As seen, the reactivity of these scFvs was markedly enhanced by Tween treatment of the blot membranes (12). Because these scFv phages were selected on a frozen-section mildly fixed by acetone, they may have preferentially reacted with renatured antigens on the membrane. A considerable number of phages with low specificity that reacted with multiple bands on muscle Western analysis

[3] M. Furuta, T. Ito, C. Eguchi, T. Tanaka, E. Wakabayashi-Takai, and K. Kaneko, unpublished result.

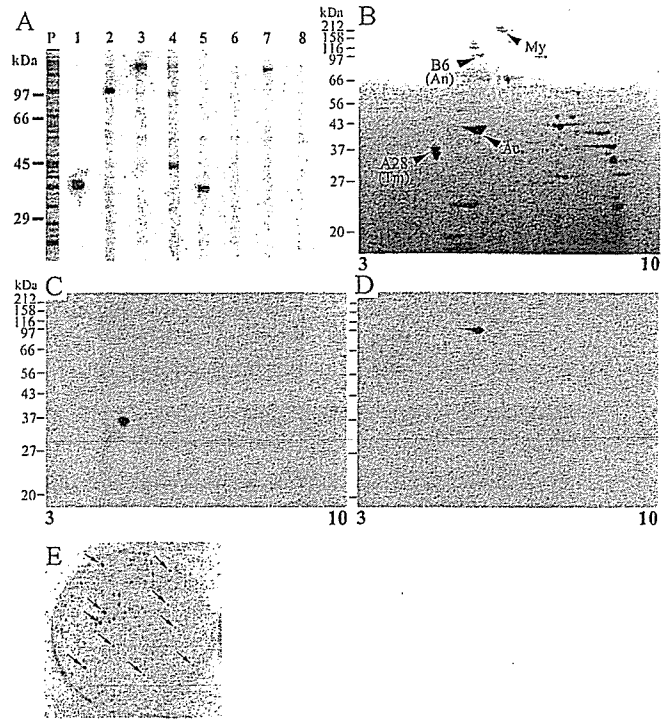

FIG. 3. **Identification of human muscle antigens by *in situ* phage screening (ISPS).** *A*, the one-dimensional Western analysis of muscle proteins by the representative scFv phages. About 2 μg of human muscle protein on each strip was reacted with scFv phages with (*lanes 1–4*) or without (*lanes 5–8*) Tween treatment. *P*, proteins on the strip visualized by colloidal gold stain (Bio-Rad). *Lanes 1* and *5*, phage A28 (5×10^9 cfu/ml); *lanes 2* and *6*, phage B6 (3×10^{10} cfu/ml); *lanes 3* and *7*, phage E2 (5×10^9 cfu/ml); *lanes 4* and *8*, phage E6 (3×10^{10} cfu/ml). *B*, Coomassie stain of human muscle proteins (60 μg) electrophoresed on a two-dimensional gel. Proteins identified by ISPS in this work are indicated by *arrowheads*: *My*, myosin heavy chain; *Ac*, α-actin; *A28*, the antigen recognized by phage A28 (tropomyosin, *Tm*); *B6*, the antigen recognized by phage B6 (α-actinin, *An*). The pH range in the first dimension (isoelectric focusing) is shown at the *bottom*. *C* and *D*, the two-dimensional Western analysis of human muscle proteins (30 μg) by using phages A28 (*C*) and B6 (*D*) at a concentration of 5×10^{10} cfu/ml. *E*, immunoscreening of a muscle expression library with phage A28. The λ plaques of the secondary screening were reacted with phage A28 (5×10^{10} cfu/ml). Positive plaques are indicated by *arrows*.

were obtained through experiments A through E (data not shown).

Identification of Muscle Antigens by using scFv Phages Obtained in ISPS—Two-dimensional Western blotting of muscle proteins was performed by using positive scFv phages, and their corresponding antigens were assigned on a Coomassie-stained two-dimensional gel (Fig. 3, *B–D*). The 42-kDa protein recognized by several clones (B85, C22, D2, E6, and E30) had a pI of 5.2 and was classified as α-actin (Fig. 3*B*, *Ac*), which accounts for about 20% of the total protein in muscle (14). Similarly, the 210-kDa antigen had a pI of 5.8 and was classified as a myosin heavy chain (Fig. 3*B*, *My*), which weighed about 40% of the total proteins in muscle (14), although it was not efficiently displayed on our two-dimensional gel system when compared with the results of a previous researcher who used agarose gel for the first dimension (15). These assignments of the 42-kDa and 210-kDa spots were confirmed both by Western analysis of the same two-dimensional blots using anti-actin or anti-myosin heavy chain mouse monoclonal antibodies (data not shown). Clone A28 recognized a doublet protein spot of 36–37 kDa with a pI of 4.7, suggesting that it reacted with more than one isoform of the antigen (Fig. 3*C*). Clone B6 recognized a single spot of 100 kDa with a pI of 5.3 (Fig. 3*D*). These antigens were also assigned to spots on the two-dimen-

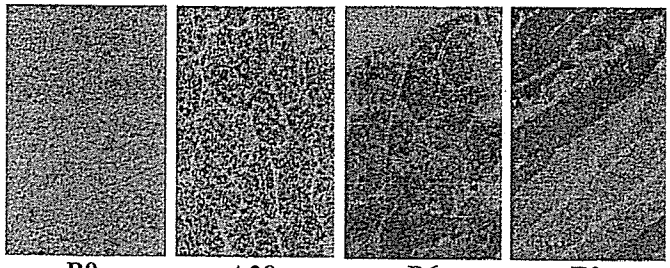

FIG. 4. **Immunostaining of human muscle sections by using scFv phages B9 (negative phage), A28 (anti-tropomyosin-α), B6 (anti-α-actinin 2), and E2 (anti-myosin heavy chain β), longitudinal section.**

TABLE IV
Features of anti-muscle scFv clones

Clone	Western	Antigen	IHC[a]	IS
	kDa			
A28	37	Tropomyosin-α	+	+
B6	100	α-Actinin 2	+	+
B85	42	α-Actin	−	ND
C22	42	α-Actin	−	ND
C43	210	Myosin heavy chain IIa	+	+
D2	42	α-Actin	−	ND
E2	210	Myosin heavy chain β	+	+
E6	42	α-Actin	+	−
E30	42	α-Actin	−	ND

[a] IHC, immunohistochemistry; IS, immunoscreening; ND, not determined.

sional gel (Fig. 3*B*, *A28* and *B6*, respectively).

Because the scFv phages A28 and B6 were highly specific, immunoscreening of a human muscle expression library (cloned in λ TriplEx vector, CLONTECH Laboratories) was performed to identify the corresponding antigens (Fig. 3*E*). We found 80 positive plaques for A28 out of 1.2×10^4 λ clones and 3 positive plaques for B6 out of 1.2×10^5 λ clones. For A28, four of the five λ inserts had a sequence that matched the human cDNA sequence of tropomyosin-α (TPM3) 100%, and the other λ insert matched the other isoform of tropomyosin-α (TPM1). For B6, all three sequences of the λ inserts completely matched the human α-actinin 2 sequence. The observed molecular masses and pI values for the two protein spots were consistent with those calculated for tropomyosin-α (33 kDa and 4.6) and α-actinin 2 (104 kDa and 5.3).

To confirm the results of immunoscreening, the 37- and 100-kDa protein spots visualized by copper-staining (Bio-Rad) were cut out, digested *in gel* with trypsin (1), and subjected to mass fingerprinting analysis with a MALDI-TOF mass-spectrometer (13). The masses of the tryptic peptides obtained for the 36- to 37-kDa protein best matched those of α- and β-tropomyosin. Similarly, a mass fingerprint of the 100-kDa protein closely matched that of α-actinin 2.

Histochemical examination revealed that scFv phages A28 (anti-tropomyosin) and B6 (anti-α-actinin) diffusely stained muscle cells (Fig. 4). Anti-myosin heavy chain phage E2 stained muscle cells in an isoform-dependent manner (Fig. 4), and another anti-myosin heavy chain phage, C43, also showed an isoform-dependent staining pattern (data not shown). As expected, the isoforms of the myosin heavy chain recognized by the phage clones C43 and E2 were identified by immunoscreening to be the myosin heavy chains IIa and β (MYH7), respectively. By contrast, only one of the five clones of anti-actin scFv phage, E6, weakly stained the muscle cells, possibly because of the low affinity of anti-actin scFvs for F-actin. The features of the anti-muscle scFvs are listed in Table IV.

DISCUSSION

We performed ISPS on a 4800-μm^2 microarea of muscle. The 40 × 40-μm area corresponded to about 0.5–1.0 transverse sections of muscle cells (see Fig. 2*C*). A single round of selection was fruitful in all of our trials (experiments A through E) to obtain specific scFvs against minute amounts of antigens present in a microarea, resulting in the identification of the muscle proteins by immunoscreening. Most of the specific scFv phages obtained here were for major muscle antigens, *i.e.* myosin heavy chain, α-actin, and tropomyosin-α, present in the reaction area. Myosin and actin are the two major constituents of muscle and account for about 40 and 20%, respectively, of the total weight of muscle protein (14). One or more tropomyosins comprise the third major protein in muscle (accounting for about 5% of the total (14)). Because the total amount of proteins in a 4-mm^2 muscle section that was 2-μm thick was measured 2.5 μg (n = 4), the amount of tropomyosin in a 4800-μm^2 microfragment was 150 pg; therefore, 31 fg = 6×10^5 molecules of tropomyosin was estimated to exist in 1-μm^2 microfragments (2-μm thick). To our surprise, we also succeeded in obtaining an scFv phage against α-actinin 2, which accounts for only 1% of muscle protein (14); hence, the total weight in 4800 μm^2 is 30 pg (similarly, 6.3 fg = 4×10^4 molecules of α-actinin/μm^2 microfragments). The reason why the scFv for such a minor component (α-actinin 2) was selected may have been the strong antigenicity of the antigen or the high abundance of one or more anti-α-actinin scFvs in the Griffin. 1 library. Another possibility is that a portion of the Z-disk, in which α-actinin is localized (16), was efficiently exposed to the reaction surface on the transverse sections.

To select scFvs against minor antigens existing in target structures, a single round, rather than multiple rounds, of selection was recommended, because positive clones could be lost during repeated rounds of selection. Presumably, changes in phage population in a phage pool through the steps of panning are affected not only by the reactivity of scFvs displayed on the phage particles but also by biological factors such as the efficiency of phage production or the growth rates of *E. coli* in each clone. High throughput analysis of the initial round of clones, which involves picking up unique clones from a large pool of redundant colonies and producing each clone phage, is a key for the further advance of ISPS.

We noted the high quality of the phage antibodies (scFvs) selected against such minute amounts of antigens *in situ* from the Griffin. 1 library. Among the phage antibodies obtained here, anti-myosin heavy chain phage antibodies are definitely specific for one or more isoforms on immunohistochemistry (Fig. 4) and immunoscreening, indicating that they are reliable for immunological examinations. As expected, many of the antibodies obtained by ISPS in this study can be used for Western analyses, immunohistochemistry, and immunoscreening (Table IV). Interestingly, the obtained phage antibodies showed higher reactivity against renatured antigens (Fig. 3*A*), suggesting that "conformation-dependent" phage antibodies can be selected by ISPS. Thus, phage antibodies that are useful for a wide variety of immunological and biochemical analyses of the target antigens could be obtained by ISPS in combination with the Griffin. 1 library. Theoretically, ISPS can also be applied to structures consisting of non-protein components, such as complex sugars and lipids. When monoclonal antibodies are obtained against non-protein components, the antigens can be identified by other methods besides immunoscreening, for example, by immunoaffinity purification.

A major technical problem encountered in this study was

that the collected target fragments tended to stick to the inside of glass capillaries. This was partially prevented by the addition of detergent to the buffer overlaid on tissues or by careful manipulation of the capillaries. Siliconization of capillaries was not effective to solve this problem. In this case, fragments collected from paraffin sections were not very sticky to glass capillaries. When the target structures were very small (less than 10 μm), we found another problem, namely that substantial amounts of the collected targets were lost during washing by centrifugation. This problem remains to be solved. On the other hand, when the target structures were rather large (100 μm or more), no such problems were encountered through the experimental steps. Relatively large targets could be collected directly into PCR reactions by using a needle under a stereomicroscope after tissue sections were washed on glass and dried. In this method, it was not necessary to overlay a buffer on tissue sections during collection or to wash the collected targets by centrifugation.

There are four factors that may affect the sensitivity of ISPS: 1) the avidity of scFv phages for their target antigen (which depends on the K_d and the valence of the displayed scFvs), 2) the phage concentration, 3) the amount of antigens involved in the reaction, and 4) the reactivity of the antigens (affected by treatment of tissue section, such as by fixation, antigen retrieval treatment, drying, or others). The proteins in paraffin sections, the most common source of tissue samples, seemed to be less reactive with scFvs, possibly due to the lower reactivity of the antigens (data not shown). It is important to find an effective method of antigen retrieval for a variety of histopathological structures when paraffin sections are used for ISPS. The scFv library can be modified to further improve the sensitivity of ISPS, because higher concentrations of individual phages are needed to detect lower amounts of antigens. Libraries with different diversities may be applied to a target structure depending on the amount of antigens to be identified.

In the last decade, applications of mass spectrometry (MS) to peptide profiling (17), protein profiling (18), and imaging of protein distribution (19) in tissue samples have been developed. The literature does not describe the amount of tissue needed for MS-based protein identification, although as little as 5 ng of protein has been identified by MS after separation on two-dimensional polyacrylamide gel electrophoresis (1). It should be pointed out, however, that ISPS was the only approach that enabled us to obtain highly specific monoclonal antibodies by using such a minute amount of tissue components. We were able to collect more than 100 target microstructures in 1 day, depending on their abundance in a tissue section. ISPS may enable the identification of even minor components of bodies, plaques, or microdeposits of unknown components in various organs or subcutaneous lesions in focal and systemic disorders. Some of these microstructures seen in neuromuscular and systemic disorders are now under investigation.

Acknowledgments—We thank Dr. Greg Winter (Medical Research Council, Cambridge, UK) for providing the Griffin. 1 library and useful comments on this work. We also acknowledge R. Kamata, K. Inugami, M. Shin, and D. Nishikiori for technical assistance. We are grateful to Drs. I. Nishino and I. Nonaka, NCNP, for arrangement of muscle samples, and Drs. S. Takashima, M. Imamura, and T. Sasaoka, NCNP, for helpful suggestions.

REFERENCES

1. Wilm, M., Shevchenko, A., Houthaeve, T., Breit, S., Schweigerer, L., Fotsis, T., and Mann, M. (1996) *Nature* **379,** 466–469
2. MacCafferty, J., Griffiths, A. D., Winter, G., and Chiswell, D. J. (1990) *Nature* **348,** 552–554
3. Nissim, A., Hoogenboom, H. R, Tomlinson, I. M., Flynn, G., Midgley, C., Lane, D., and Winter, G. (1994) *EMBO J.* **13,** 692–698
4. Winter, G., Griffiths, A. D., Hawkins, R. E., and Hoogenboom, H. R. (1994) *Annu. Rev. Immunol.* **12,** 433–455
5. Hoogenboom, H. R., de Bruine, A. P., Hufton, S. E., Hoet, R. M., Arends, J. W., and Roovers, R. C. (1998) *Immunotechnology* **4,** 1–20
6. Lehmann, U., Bock, O., Glockner, S., and Kreipe, H. (2000) *Pathobiology* **68,** 202–208
7. Simone, N. L., Paweletz, C. P., Charboneau, L., Petricoin, E. F., 3rd, and Liotta, L. A. (2000) *Mol. Diagn.* **5,** 301–307
8. Griffiths, A. D., Williams, S. C., Hartley, O., Tomlinson, I. M., Waterhouse, P., Crosby, W. L., Kontermann, R. E., Jones, P. T., Low, N. M., Allison, T. J., Prospero, T. D., Hoogenboom, H. R., Nissim, A., Cox, J. P. L., Harrison, J. L., Zaccolo, M., Gherardi, E., and Winter, G. (1994) *EMBO J.* **13,** 3245–3260
9. Goletz, S., Christensen, P. A., Kristensen, P., Blohm, D., Tomlinson, I., Winter, G., and Karsten, U. (2002) *J. Mol. Biol.* **315,** 1087–1097
10. Coomber, D. W. J. (2002) *Methods Mol. Biol.* **178,** 133–145
11. Sambrook, J., Fritsch, E. F., and Maniatis, T. (1989) *Molecular Cloning: A Labolatory Manual*, 2nd Ed., Cold Spring Harbor Laboratory, Cold Spring Harbor, NY
12. Van Dam, A. P., Van den Brink, H. G., and Smeenk, R. J. T. (1990) *J. Immunol. Methods* **129,** 63–70
13. Kinumi, T., Tobin, S. L., Matsumoto, H., Jackson, K. W., and Ohashi, M. (1997) *Eur. Mass Spectrom.* **3,** 367–378
14. Ohtsuki, I., Maruyama, K., and Ebashi, S. (1986) *Adv. Protein Chem.* **38,** 1–67
15. Hirabayashi, T. (2000) *Electrophoresis* **21,** 446–451
16. Masaki, T., Endo, M., and Ebashi, S. (1967) *J. Biochem.* **62,** 630–632
17. Jimenez, C. R., Li, K. W., Dreisewerd, K., Spijker, S., Kingston, R., Bateman, R. H., Burlingame, A. L., Smit, A. B., van Minnen, J., and Geraerts, W. P. M. (1998) *Biochemistry* **37,** 2070–2076
18. Chaurand, P., Stoeckli, M., and Caprioli, R. M. (1999) *Anal. Chem.* **71,** 5263–5270
19. Stoeckli, M., Chaurand, P., Hallahan, D. E., and Caprioli, R. M. (2001) *Nature Med.* **7,** 493–496

Solid-state NMR studies of the secondary structure of a mutant prion protein fragment of 55 residues that induces neurodegeneration

David D. Laws*†, Hans-Marcus L. Bitter*†, Kai Liu*‡, Haydn L. Ball§, Kiyatoshi Kaneko§, Holger Wille§, Fred E. Cohen¶, Stanley B. Prusiner§, Alexander Pines*†, and David E. Wemmer*‡‖

*Department of Chemistry, University of California, Berkeley, CA 94720; †Materials Sciences Division and ‡Physical Biosciences Division, Lawrence Berkeley National Laboratory, 1 Cyclotron Road, Berkeley, CA 94720; and Departments of §Neurology and ¶Biochemistry and Biophysics, University of California, San Francisco, CA 94143

Contributed by Alexander Pines, August 1, 2001

The secondary structure of a 55-residue fragment of the mouse prion protein, MoPrP(89–143), was studied in randomly aggregated (dried from water) and fibrillar (precipitated from water/acetonitrile) forms by ^{13}C solid-state NMR. Recent studies have shown that the fibrillar form of the P101L mutant of MoPrP(89–143) is capable of inducing prion disease in transgenic mice, whereas unaggregated or randomly aggregated samples do not provoke disease. Through analysis of ^{13}C chemical shifts, we have determined that both wild-type and mutant sequence MoPrP(89–143) form a mixture of β-sheet and α-helical conformations in the randomly aggregated state although the β-sheet content in MoPrP(89–143, P101L) is significantly higher than in the wild-type peptide. In a fibrillar state, MoPrP(89–143, P101L) is completely converted into β-sheet, suggesting that the formation of a specific β-sheet structure may be required for the peptide to induce disease. Studies of an analogous peptide from Syrian hamster PrP verify that sequence alterations in residues 101–117 affect the conformation of aggregated forms of the peptides.

It is now widely accepted that the prion diseases, such as Creutzfeldt-Jakob disease and Gerstmann-Straussler-Scheinker disease in humans and bovine spongiform encephalopathy, are caused by a conformational change of the prion protein (PrP) from a normally folded cellular form, PrP^C, to an alternate, aggregation-prone, pathogenic scrapie form, PrP^{Sc} (1, 2). In sporadic and inherited forms of these diseases, initiation is thought to occur through spontaneous conversion of endogenous PrP^C to PrP^{Sc}, which then autocatalytically propagates. Remarkably, PrP^{Sc} can be introduced into a naive host where it can initiate this autocatalytic propagation; this paradigm describes the infectious forms of prion diseases. Although PrP^C and PrP^{Sc} have identical amino acid sequences, the two isoforms have profoundly different secondary, tertiary, and quaternary structures as observed by CD, Fourier-transform IR, and limited proteolysis (3–7). PrP^C is primarily α-helical and monomeric whereas PrP^{Sc} is much richer in β-sheet and is oligomeric. It is known that a variety of sequence variants lead to a much higher probability of disease, presumably by facilitating the initial conversion of PrP^C to PrP^{Sc}. The sites of variation are distributed rather widely through the protein, including some in the well-folded regions of the solution structure of PrP^C whereas others are in poorly ordered regions. Knowing the structures of both isoforms and understanding the relationship between sequence and the ability to convert between structures are vital to understanding the process of structural transformation from PrP^C to PrP^{Sc}.

The structure of an unglycosylated form of PrP^C has been determined by solution NMR (3, 5, 6) (Fig. 1); however, less is currently known about the structure of PrP^{Sc}, primarily because purified PrP^{Sc} is isolated as insoluble aggregates. When PrP^{Sc} is subjected to limited proteolysis, it becomes N-terminally truncated to form PrP 27–30. Preparations of PrP 27–30 are infectious and contain *para*-crystalline fibrils exhibiting the properties of amyloid, which cannot be studied by conventional techniques for structure determination such as x-ray crystallography or solution NMR. Attempts to carry out *in vitro* conversion of PrP^C to PrP^{Sc} on a large scale have been unsuccessful. For this reason there have been attempts to recapitulate the behavior of the whole protein with fragments (peptides). Recently, Kaneko *et al.* (8) have worked with mice expressing low levels of PrP (MoPrP) carrying the P101L mutation, which causes Gerstmann-Straussler-Scheinker disease in humans, and causes disease in mice when expressed at high levels. They showed that a synthetic 55-aa fragment of MoPrP, residues 89–143 with the P101L mutation, can form β-rich, fibrillar aggregates that stimulate disease when inoculated into these animals, whereas the peptide in nonfibrillar form does not (8). Thus, MoPrP (89–143, P101L) presents an opportunity to gain insight into the structural features associated with the ability to cause disease and to learn about the mechanism of conversion from PrP^C to PrP^{Sc}.

Numerous studies support the notion that the key region of PrP in the conversion process includes residues 89–143. The N terminus of protease-resistant PrP 27–30 is at residue 90, defining the approximate start of the infectious domain (9). A Japanese male with an amber mutation at residue 145 died of prion disease, thereby suggesting that the last 87 residues of PrP are not crucial for the initial formation or propagation of PrP^{Sc} (10), although multiple attempts to transmit prions form the brain of this patient to experimental animals have been unsuccessful. A mini-prion has been created containing residues 89–140 linked to 176–231 (11) and demonstrated to cause a transmissible neuropathologically accurate prion disease in transgenic mice. Moreover, deletion of residues 90–145 has been shown to prevent PrP^{Sc} formation (12). Various fragments in this region have been shown to fold into α-helix- or β-sheet-rich conformations depending on the conditions under which they were prepared (13–20). Thus, there is considerable data to suggest that the region from residue 90 to 143 has substantial conformational lability and plays a significant role in the conversion from PrP^C to PrP^{Sc}.

In this work, we describe experiments using solid-state NMR to study the secondary structure of PrP (89–143) before and after conversion to the active, fibril-rich, aggregated state. Unlike solution NMR or x-ray crystallography, solid-state NMR can provide structural information for samples in ordered states,

Abbreviations: PrP, prion protein; MoPrP, mouse PrP; SHaPrP, Syrian hamster PrP; wt, wild type; PrP^C, Prp cellular form; PrP^{Sc}, PrP scrapie form; MAS, magic-angle spinning; CP, cross-polarization.

‖To whom reprint requests should be addressed at: Department of Chemistry, MC-1460, University of California, Berkeley, CA 94720. E-mail: dewemmer@LBL.gov.

The publication costs of this article were defrayed in part by page charge payment. This article must therefore be hereby marked "*advertisement*" in accordance with 18 U.S.C. §1734 solely to indicate this fact.

www.pnas.org/cgi/doi/10.1073/pnas.201404298

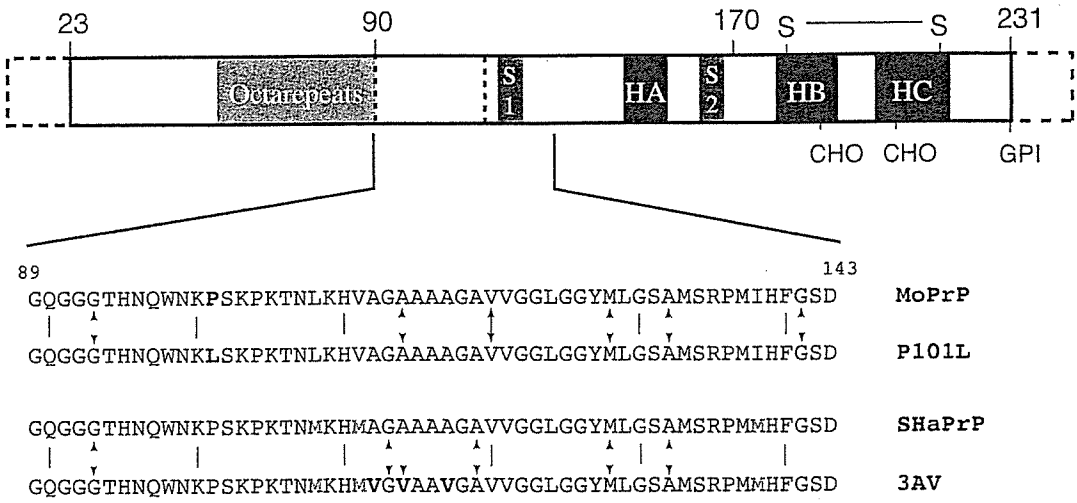

Fig. 1. A schematic diagram of the PrP showing the sequence motifs and secondary structure of PrP^C. The segment marked octarepeats contains six copies of an eight-residue repeat sequence, S1 and S2 are the two small β-strands, and HA, HB, and HC designate the three helices. Residues 1–23 are processed off during transport. The points marked CHO indicate the sites at which oligosaccharides are attached *in vivo*, and GPI indicates the attachment point of the membrane anchor. The region 23–124 is unstructured in PrP^C in solution. Below the sequences of peptides studied are given, and the sites of sequences variations are highlighted. Sites of incorporation of isotope labels are indicated by arrows.

such as aggregated peptides and proteins, through the use of chemical-shift information and the determination of internuclear distances. It is well established that ^{13}C and ^{15}N chemical shifts in peptides and proteins are quite sensitive to local secondary structure (21–24). For example, the isotropic chemical shifts of a C_α in an α-helix versus a β-sheet can differ by more than 8 ppm. Thus, ^{13}C chemical shifts can provide insight into the local secondary structure and can be used in characterizing the secondary structure of the PrP fragments. By placing ^{13}C labels in six residues spread throughout the 55-residue peptide, the secondary structure was monitored in both the wild-type (wt) and P101L mutant forms of MoPrP(89–143). Solid-state ^{13}C NMR spectra of both the wt and P101L peptides exhibit a mixture of helical and extended conformation resonances, indicating substantial conformational heterogeneity and lability in the nonfibrillar state. After aggregation in an acetate-buffered acetonitrile/water solution, the solid-state ^{13}C NMR spectrum of the P101L peptide loses all of the helical peaks, suggesting that the mutation affects not only the local secondary structure, but also the overall structure of the fragment. Similar structural plasticity and long-range conformational effects caused by mutations also were observed in the equivalent hamster sequence fragment with three alanine-to-valine (3AV) mutations at positions 112, 114, and 117, a sequence region previously shown to have structural plasticity (19). Mice carrying the 3AV transgene develop a spontaneous and rapidly lethal condition with neuropathology consistent with a prion disease.

Experimental Procedures

The ^{13}C isotopic labels incorporated into PrP peptides were selected on the basis of their isotropic chemical-shift ranges (22) so that the ^{13}C sites would be resolvable in a one-dimensional NMR spectrum. All peptides were synthesized by using optimized fluorenylmethoxycarbonyl (Fmoc) chemistry on an Applied Biosystems 433 peptide synthesizer. Fmoc amino acid derivatives were preactivated by reaction with 2-(^{1}H-benzotriazol-1-yl)-1,1,3,3-tetramethyluronium hexafluorophosphate and diisopropylethylamine. After the coupling of each amino acid, a capping step was performed by using *N*-(2-chlorobenzyloxycarbonyloxy) succinimide (Nova Biochem). Labeled residues were coupled manually by using a 1.5-fold excess of amino acid, and coupling efficiency was monitored by using the quantitative ninhydrin test. The peptide was deprotected and cleaved from the resin in 1:2:2:35 ethanedithiol/thiophenol/thioanisole/95% trifluoroacetic acid after removal of the N-terminal Fmoc group. The crude peptide was precipitated with diethyl ether and then redissolved in 8 M guanidine hydrochloride before purification by semipreparative C_4 reversed-phase HPLC at 50°C on a Rainin Instruments liquid chromatography system. The identity of the purified peptides was confirmed by electrospray MS using a Perkin–Elmer-Sciex API-300 instrument.

Randomly aggregated peptide was generated by drying a water solution of the peptide by blowing a stream of dry nitrogen over it until it was macroscopically dry. To convert the P101L and 3AV peptides to a fibrillar state, the samples were dissolved in a 50:50 (vol/vol) mixture of acetonitrile and acetate-buffered saline (100 mM NaCl, 20 mM NaOAc, pH 5.0). The solution then was allowed to sit undisturbed for ≈3 weeks. The solution gradually grew cloudy as an insoluble aggregate collected. Aggregation was judged complete at ≈3 weeks, after which the suspension was sedimented in an ultracentrifuge to collect the solid material. The supernatant was removed and the gelatinous pellet was dried overnight by blowing gaseous nitrogen over the sample. Electron microscopy was used as described (20) to verify the presence of fibrils in the aggregated forms.

All ^{13}C NMR spectra were obtained either at 7.07 Tesla (corresponding to a ^{13}C Larmour frequency of 75.74 MHz) on a custom spectrometer based on a Tecmag (Houston) pulse programmer with a Chemagnetics–Otysuka Electronics (Fort Collins, CO) 4-mm double-resonance magic-angle spinning (MAS) probe, or at 11.72 Tesla (corresponding to a ^{13}C Larmor frequency of 125.75 MHz) on a triple-resonance Varian/Chemagnetics Infinity spectrometer with a 4-mm T3 triple-resonance MAS Chemagnetics probe. For spectra obtained at 7.07 Tesla, the cross-polarization (CP) contact time was 2.0 ms, the ^{1}H decoupling field strength was 91 kHz, and the recycle delay was 1.0 sec. For spectra obtained at 11.72 Tesla, the CP contact time was 2.0 ms, the ^{1}H decoupling field strength was 114 kHz, and the recycle delay was 1.0 sec. A spectrum of the fibrillar MoPrP 89–143 P101L also was obtained with two-pulse phase-modulation decoupling (25). Isotropic shift values were measured relative to the carbonyl carbon of glycine at 176.04 ppm in an external reference sample of glycine.

Table 1. ^{13}C labels used to study the secondary structure of PrP peptides

Label	Shift range, ppm
G93 C_α	43—44
G113, 141 C_0	168—172
V114, 120 C_α	56—66
A114, 119 C_α	46—54
A132 C_β	14—22
M128 C_0	170—176

Results and Discussion

The ^{13}C labels that were incorporated into MoPrP(89–143) are listed in Table 1 along with the expected chemical-shift ranges for each label. Different amino acid labels were used to minimize spectral overlap and to allow assignment of the different resonances. The locations of the isotopic labels were chosen so that the secondary structure of the peptide could be monitored at points distributed although much of the peptide. Fig. 2*A* shows a ^{13}C CPMAS spectrum of the wt MoPrP(89–143) peptide. Resonance assignments were based on published ^{13}C solid-state chemical-shift ranges (22). The distribution of shifts in the spectrum, including multiple lines for some sites, of the wt MoPrP(89–143) peptide indicates a mixture of helical and extended (β-sheet-like) conformers (identified in Fig. 2*A*). For V120 it is quite clear that there is a continuous distribution of shifts, indicating substantial conformational heterogeneity although extended conformers are predominant, which also seems to be the case for A132. For A114, both helical and extended conformation resonances are present, but with nearly equal intensity. Together these results indicate that the sample was not merely a mixture of helical and extended peptides, but peptides that adopt a variety of mixed secondary structures, i.e., microscopically disordered. This conformational heterogeneity in the solid state is not unexpected, given that solution NMR results suggest that PrP(89–143) is generally unstructured in solution (data not shown), as is the equivalent Syrian hamster (SHa) peptide (17) and smaller peptides from this part of the protein also had displayed conformational variability (19).

In Fig. 2, the solid-state ^{13}C NMR spectrum of wt MoPrP(89–143) is compared with the equivalent spectra of the mutant MoPrP(89–143, P101L) peptide both before (Fig. 2*B*) and after (Fig. 2*C*) conversion to the aggregated, fibrillar state. The chemical shifts of peaks in these spectra are listed in Table 2. The effects of the point mutation on the secondary structure of the peptide are quite significant; the intensities of the helical resonances for all of the ^{13}C labels decrease, regardless of their location in the peptide. This effect is most striking for the $^{13}C_\alpha$ label in A114, for which the ratio of helix to β-sheet changes from ≈1:1 in the spectrum of the wt peptide to ≈1:2 in the spectrum of the P101L mutant. These results confirm that the PrP(89–143) fragment is structurally pliable and highly sensitive to mutations because a single amino acid substitution gives rise to conformational changes throughout the peptide, including amino acids over 30 residues away from the P101L substitution, as evidenced by the changes at A132.

Upon aggregation, the P101L mutant peptide appears to convert completely to an extended, β-sheet-like form, as seen in Fig. 2*C*. However, the resonances in the spectrum of the fibrillar P101L peptide (Fig. 2*C*) appear broader than the randomly aggregated P101L peptide (Fig. 2*B*). The most likely explanation is that there is a distribution of extended conformations present, which would account for what appear to be shoulders on the A114 and G93 $^{13}C_\alpha$ resonances. In an attempt to better resolve these resonances, another spectrum of the aggregated P101L peptide also was obtained by using two-pulse phase-modulation

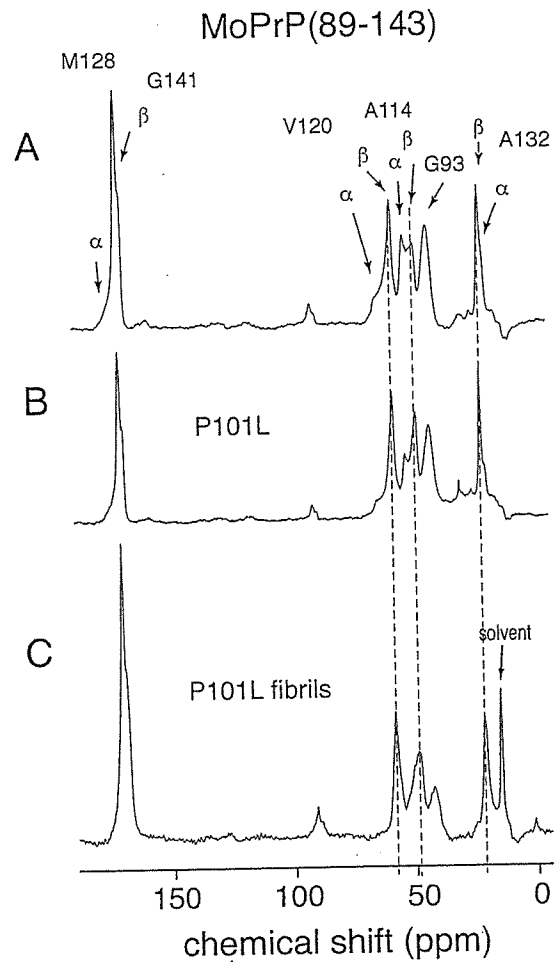

Fig. 2. One hundred twenty-six-megahertz solid-state ^{13}C CPMAS spectra of wt mouse PrP(89–143) obtained at a spinning speed of 10 kHz. (*A*) wt MoPrP(89–143) spectrum, with the sample dried from water. Arrows indicate the resonances, which occur at characteristic shifts for helical and extended (sheet) conformations. The resonance from the carbonyls of G141 in a helical conformation and M128 in the extended conformation overlap, and so cannot be distinguished. (*B*) Spectrum of MoPrP(89–143, P101L) dried from water. (*C*) Spectrum of MoPrP(89–143, P101L) peptide after conversion to fibrillar form by precipitation from acetonitrile/water. The lines superimposed over the resonances for V120, A114, and A132 mark the β-sheet chemical shifts. The higher ratio of β-sheet to helical resonances in the unaggregated mutant MoPrP(89–143, P101L) indicates the preference for this mutant to adopt β-sheet structures. This preference for β-sheet structures was enhanced by exposure of the mutant peptide to acetonitrile/water (*C*) where the helical resonances have almost disappeared.

(25) to improve ^1H decoupling and narrow the ^{13}C resonances. The A114 $^{13}C_\alpha$ resonance remained broadened, supporting the idea that there are multiple extended conformations. The downfield shoulder of the A114 $^{13}C_\alpha$ resonance has a chemical shift that lies between those expected for a random coil and a β-sheet conformation (Table 2), which may reflect the presence of peptides in the aggregate that is irregular in structure. This finding is consistent with the observation of Kaneko *et al.* (8) that not all of the aggregated peptide is present in fibrillar form, and that a distribution of fibril lengths was present in the sample of the aggregated P101L peptide used for this study. Despite the presence of nonfibrillar peptide, the spectra show that β-sheet conformers are most highly populated and must reflect the dominant fibrillar form.

In addition to the P101L mutant of MoPrP(89–143), we examined the equivalent peptide from the SHaPrP sequence